How "mixing" affects propagation and structure of intensely turbulent, lean, hydrogen-air premixed flames

Yuvraj[a], Hong G. Im[b], Swetaprovo Chaudhuri[a,*]

[a]*Institute for Aerospace Studies, University of Toronto, Toronto, Canada*
[b]*Clean Combustion Research Center, King Abdullah University of Science and Technology, Thuwal, Saudi Arabia*

Abstract

Understanding how intrinsically fast hydrogen-air premixed flames can be rendered much faster in turbulence is essential for the systematic development of hydrogen-based gas turbines and spark ignition engines. Here, we present fundamental insights into the variation of flame displacement speeds by investigating how the disrupted flame structure affects speed and vice-versa. Three DNS cases of lean hydrogen-air mixtures with effective Lewis numbers (Le) ranging from about 0.5 to 1, over Karlovitz number (Ka) range of 100 to 1000 are analyzed. Suitable comparisons are made with the closest canonical laminar flame configurations at identical mixture conditions and their appropriateness and limitations in expounding turbulent flame properties are elucidated. Since near zero-curvature surface locations are most probable and representative of the average flame geometry in such large Ka flames, statistical variation of the flame displacement speed and concomitant change in flame structure at those locations constitute the focus of this study. To that end, relevant flame properties are averaged in the direction normal to the zero-curvature isotherm locations to obtain the corresponding conditionally averaged flame structures. For the leanest and smallest Le case, downstream of the most probable zero-curvature regions, the temperature increases beyond those of the standard laminar flame, leading to enhanced local thermal gradient and flame speed. These result from increased heat-release rate contribution by preferential diffusion in positive curvatures downstream of the zero-curvature locations. Furthermore, for all cases, lo-

*Corresponding author
Email address: swetaprovo.chaudhuri@utoronto.ca (Swetaprovo Chaudhuri)

cally, the flame structure is also broadened due to reversal in the direction of the flame speed gradient underpinned by ubiquitous, non-local, cylindrical flame-flame interaction upstream of the zero-curvature regions, resulting in localized scalar mixing within the flame structure. The combined effect of these two non-local phenomena results in the most probable flame structure and the associated variation of the local flame speed of a premixed flame in turbulence.

Keywords: flame displacement speed, turbulent premixed flames, lean hydrogen flames, flame-flame interaction

---

Novelty and Significance Statement

The paper presents fundamental discoveries pertaining to the structure and propagation of intensely turbulent, lean premixed hydrogen-air flames, emerging from the analysis of averaged flame structures conditioned to zero-curvature surface locations. These locations are most probable alongside corresponding to the mean of curvature distribution. Analysis of such structures reveals how non-local effects determine the average flame displacement speed, for the first time. Non-local effects appear in fluid turbulence literature but rarely in turbulent combustion. The paper shows that non-local effects within the flame structure address long-standing questions on how premixed flames are broadened in turbulence and why local flame displacement speeds of ultra-lean hydrogen-air flames are ubiquitously higher than their standard laminar counterpart.

Author Contributions

- Y performed research, analyzed data, wrote the paper
- HGI performed research, wrote the paper
- SC designed research, performed research, wrote the paper

1. Introduction

Hydrogen is considered a promising alternative fuel to achieve sustainable energy solution for both transportation and stationary applications. Ultra-lean premixed combustion of hydrogen has the potential of achieving high efficiency and low NO_x emissions [1], but some critical challenges need to be overcome before its full implementation in practical engineering systems. One notable issue is the extremely high flame speed that often occurs erratically, in the presence of strong turbulence, leading to flashback and damage to the gas turbine injector system. A similar situation is encountered for SI engines where high flame speed and reactivity of stratified hydrogen-air mixtures may result in pre-ignition or knocking.

Earlier studies on local flame displacement speeds investigated the effect of local curvature [2–9] and strain [2, 5, 10], Lewis number [11–14], and thickness [15] in the context of turbulent flames. Consumption speeds of ultra-lean hydrogen-air turbulent premixed flames were comprehensively studied [16] and compared with canonical laminar flame configurations, focusing on positive curvatures. Furthermore, the importance of zero-curvature regions was emphasized and the departure of averaged local consumption speed behavior of high Ka turbulent flames from that of the strained laminar flames was highlighted [17]. A recent study for lean hydrogen-air flames [18] reported that both freely propagating and turbulent flames of lean hydrogen-air mixtures demonstrated similar thermo-diffusive responses in moderate Ka regimes. The positively curved regions on the flame surface were characterized with higher equivalence ratios and higher consumption speeds. It was also argued that enhanced temperatures and consumption speed in zero-curvature regions occurred due to higher heat release rate in the upstream, preceding positive curvature regions.

Recent Lagrangian analysis tracked the evolution of flame surface points or flame particles [19] from their genesis at positively curved leading regions [17, 20, 21] to annihilation at negatively curved trailing regions [22]. It was shown that for moderate Ka, near-unity Le flames, flame-flame interaction leading to annihilation at large negative local curvatures κ results in very large excursions of the density-weighted flame displacement speed $\widetilde{S}_d = \rho_0 S_d/\rho_u$ over its unstretched, standard laminar value S_L [22]. Here, ρ_u and ρ_0 are the density of the reactant mixture and the density at the isotherm of interest, T_0, within the flame structure. Once such local self-interaction begins, the enhanced $\widetilde{S}_d$ leads to larger negative κ, resulting in enhanced

$\widetilde{S}_d$. This fast-paced process continues until the flame surface is annihilated. The local flame structure differs greatly from an unstretched standard laminar flame during the interactions. Given the distinct transient structure, the steady weak stretch theory [23–25] falls short in explaining the aforementioned enhanced $\widetilde{S}_d$ at large negative curvatures. As such, an interacting flame theory was proposed to model the $\widetilde{S}_d$ at large negative curvatures [22] as:

$$\widetilde{S}_d = -2\widetilde{\alpha}_0\kappa \tag{1}$$

where $\widetilde{\alpha}_0$ is the density-weighted thermal diffusivity, α_0 defined at T_0, the isotherm of interest. The proposed model Eq. (1), a linear function of the local curvature, could capture the behavior of $\widetilde{S}_d$ at large negative curvatures $\kappa \ll 0$. Linear scaling with curvature had been previously proposed [26, 27] without the pre-factor 2. Flame-flame interactions at large negative curvatures are an important phenomenon in their own right since, typically, the large heat-release fluctuation resulting from rapid flame annihilation leads to sound generation [28, 29].

Flame surfaces undergoing self-interactions have been shown to form a variety of local topologies [29–33]. Extremely large negative and positive curvatures led to tunnel closure and tunnel formation, respectively. Haghiri et al. [33] found enhanced S_d during island burnout, pinch-off and tunnel formation. When the Ka is small, such interactions are infrequent and limited to rare localized events. However, increasing Ka makes such interactions frequently encountered among individual iso-scalar surfaces. As such, at $Ka \sim \mathcal{O}(1000)$, localized flame-flame interaction characterized by $\kappa\delta_L \leq -1$ was prevalent in about 44% of the flame structure [34].

Considering its significance, a theoretical analysis of the interacting preheat zones of cylindrical, laminar, premixed, inwardly propagating flame (IPF) extended and quantified [22] the curvature-based scaling of flame displacement speed [26]. As mentioned above, at very large Ka, the self-interactions become highly frequent and localized at the iso-surface level [34], but the curvature-based scaling was found to remain valid statistically [35]. In view of this, the surprising finding that a simple 1D laminar flame model could successfully describe the statistically averaged flame speed characteristics at large negative κ in turbulence may be justified by several factors. First, flame-flame interaction is a fast event during which the local turbulence

remains frozen. Moreover, at substantial curvature values, local flame structures assume length scales comparable to or smaller than the Kolmogorov scales. Finally, turbulence folds the propagating flame surfaces into a locally cylindrical form [34, 36, 37] hence large curvature surfaces in turbulence are typically cylindrical. Thus an IPF configuration serves as a canonical model to describe the statistical behavior of $\langle \widetilde{S}_d | \kappa \rangle$ for large negative curvatures undergoing flame-flame interaction.

Most importantly, such flame-flame interaction at the entire flame structure level or the internal isotherm level leads to vanishing scalar gradients and could be considered an internal *mixing* process, resulting in the broadening of the internal flame structure. Broadening of the flame structure or the separation between the iso-surfaces within the structure is proportional to $1/|\boldsymbol{\nabla} Y|$, where $\boldsymbol{\nabla} Y$ is the gradient of the iso-scalar based on mass fraction Y [38, 39]. Previous works [38, 40–44] reported substantial broadening in the preheat zone with a comparatively low broadening in the reaction zone, even under extreme Ka conditions extending to the distributed regime. This was shown by a high probability of lower valued scalar gradient generated by strong mixing in the preheat zone when compared to the reaction zone. A comprehensive review of flame structure and scalar gradients for highly turbulent premixed flames have been presented in [45]. While the flame was broadened overall, regions with scalar gradients larger than the corresponding laminar counterpart were also found on the flame surface. Su and Clemens [46] experimentally investigated two-dimensional and three-dimensional scalar dissipation rate χ fields for planar propane jet. It was shown that the negative skewness of the χ probability density function is its characteristic rather than an artifact of the experiment. Chaudhuri et al. [47] reported the flame being thinned on average from reactants to products for lean H_2-air slot jet flame. This contrasting observation was attributed to the configuration of the flame, i.e., the effect of strong shear turbulence.

In the present work, we examine how non-local effects from self-interacting flame surfaces at large negative curvatures and the associated mixing, combined with the non-local preferential diffusion at large positively curved regions, determine the local flame structure at zero-curvature, influencing the local flame speed. To that end, we analyze three direct numerical simulation (DNS) datasets at different Lewis and Karlovitz number conditions. The present flames are apparently free from the periodic cellular structures resulting from diffusive-thermal instability due to structural disruption by turbulence at very large Ka [48–50], while recognizing that thermo-diffusive

effects synergistically works with turbulence to affect flame structure and propagation [51]. Recent literature has comprehensively explored diffusive-thermal instability of hydrogen flames [18, 43, 51–53] and has shown how preferential diffusion of hydrogen and associated radicals increase consumption and displacement speeds. We focus on the negative and zero-curvature regions and find a strong enhancement of flame displacement speed in both locations for the ultra-lean case. One of the crucial findings is that, in the zero-curvature regions such enhancement is due to increased heat release in the positively curved downstream locations within the conditionally averaged flame structure. Such structures have been generated by averaging flame properties along normal directions from zero-curvature locations on an isotherm. Furthermore, such enhancement is accompanied by local broadening due to mixing effected by non-localized flame-flame interactions in the neighboring, upstream locations within the flame.

2. Methodology

The parameters of the DNS cases comprising of statistically planar, lean H_2-air turbulent premixed flame at atmospheric pressure are presented in Table 1. Le05Ka100 and Le1Ka100 represent new datasets computed using an open-source reacting flow DNS solver called the Pencil Code [19, 20, 22, 56]. Case Le08Ka1000 was previously generated and investigated [34, 35, 43] (named as F2 in these references) but included here for additional insights. All the standard laminar values are obtained from Chemkin-Premix calculations. It is to be noted that for the leanest mixture case Le05Ka100, while the standard laminar values obtained are justifiably treated as reference values, they cannot be realistically obtained from experiments due to intrinsic thermo-diffusive instability. The cases vary in equivalence ratio, ϕ and consequently the Lewis number [54], Le which is given by:

$$Le = \begin{cases} \frac{Le_O + \mathcal{A} Le_F}{1+\mathcal{A}} & \phi < 1, \\ \frac{Le_F + \mathcal{A} Le_O}{1+\mathcal{A}} & \phi > 1, \end{cases} \tag{2}$$

where

$$\mathcal{A} = \begin{cases} 1 + \beta(\phi^{-1} - 1) & \phi < 1, \\ 1 + \beta(\phi - 1) & \phi > 1. \end{cases} \tag{3}$$

The combination of selected integral length scale L_{11} [55] and root-mean-square velocity u_{rms} result in a Karlovitz number, $Ka \sim \mathcal{O}(100)$ for Le05Ka100

Parameters	Le05Ka100	Le08Ka1000	Le1Ka100
T_u [K]	310	300	310
ϕ	0.4	0.7	0.81
Le [54]	0.48	0.76	0.93
Domain dimensions [cm]	2.40	0.43	1.12
	×0.60	×0.15	×0.28
	×0.60	×0.15	×0.28
Grid points	800	1645	1120
	×200	×560	×280
	×200	×560	×280
Integral length scale [55], L_{11} [cm]	0.3	0.03	0.11
Root mean square velocity, u_{rms} [cm/s]	507.7	4746.7	1893.9
Kolmogorov length scale, η [μm]	19.9	2.141	6.5
Karlovitz no., Ka	115.4	1125.7	100.1
Reynolds no., Re_t	799.6	699.5	996.2
Damköhler no., Da	0.25	0.02	0.32
S_L [cm/s]	25.23	135.62	183.82
δ_L [cm]	5.98E-02	3.54E-02	3.53E-02
$\Delta x/\eta$	1.51	1.22	1.55
$\delta_L/\Delta x$	19.95	136.2	35.3
δt [μs]	2E-3	1E-03	2E-03

Table 1: Details of the parameters for the three 3D DNS cases investigated in this paper. For all the cases, $P = 1$ atm, $\delta_L = (T_b^\circ - T_u)/|\nabla T|_{max}$.

and Le1Ka100 whereas $Ka \sim \mathcal{O}(1000)$ for Le08Ka1000. Here, $Ka = \tau_f/\tau_\eta$ is defined as the ratio of flame time scale, $\tau_f = \delta_L/S_L$, and the Kolmogorov time scale τ_η in the unburnt mixture. $\delta_L = (T_b^\circ - T_u)/|\nabla T|_{max}$ is the standard laminar flame thickness with T_b° is the adiabatic flame temperature and S_L is the corresponding standard laminar flame speed. Reynolds number $Re = u_{rms}L_{11}/\nu \sim 700 - 1000$ for all the cases. For the present scope of work, the leanest case, Le05Ka100, with $Le = 0.48$, is of particular interest.

The Pencil Code [56] solves the governing equations of mass, momentum, energy and species conservation using a sixth-order central difference scheme to discretize all spatial terms, except for the convective terms, for which a fifth-order upwind scheme is used. A low-storage, third-order accurate Runge-Kutta RK3-2N scheme is used for time marching. A detailed chemical mechanism with 9 species and 21 reactions by [57] was used to model the H_2-air chemistry. The simulation was carried out in two stages (cases Le05Ka100 and Le1Ka100). First, homogeneous isotropic turbulence is generated in

a cube comprising of the reactant mixture. The Re_t and Ka reported in Table 1 are computed for this cube. Next, this turbulent reactant mixture is superimposed on the mean flow and fed through the inlet of a cuboidal domain to interact with a planar laminar premixed flame imposed in the initial field. The Navier-Stokes characteristic boundary conditions (NSCBC) were imposed in the inflow and outflow direction of the cuboid, with periodic boundary conditions in the transverse directions.

As for the model analysis, two additional simulations are performed for each of the DNS cases under similar conditions. (1) One-dimensional simulations for cylindrical, laminar, premixed, inwardly propagating flames (IPF) using the Pencil Code. The detailed methodology followed for the IPF simulation has been discussed by Yuvraj et al. [34]. (2) Symmetric, laminar, premixed, counter flow flames (CFF) [58] with reactant mixtures entering from both inlets at varying inlet velocities for the latter using Chemkin. It is ensured that both solvers produce identical solutions to the standard laminar case.

In the present study, we employ isotherms to represent the flame surface within the flame structure. The local flame-displacement speed S_d can be evaluated from the DNS fields using temperature as an iso-scalar surface from the right-hand side of the energy equation (Eq. (4)) as:

$$S_d = \frac{1}{\rho C_p}\left[\frac{\nabla\cdot(\lambda'\nabla T)}{|\nabla T|} - \frac{\rho\nabla T\cdot\sum_k(C_{p,k}V_kY_k)}{|\nabla T|} - \frac{\sum_k h_k\dot{\omega}_k}{|\nabla T|}\right] \tag{4}$$

where λ', V_k, h_k and $\dot{\omega}_k$ are the thermal conductivity of the mixture, the molecular diffusion velocity, enthalpy, and net production rate of the kth species at a given isotherm, respectively. $C_{p,k}$ and C_p are the constant-pressure specific heat for the kth species and for the bulk mixture, respectively. All three DNS are computed with mixture averaged diffusivity neglecting the Soret effect as in [18, 53]. Soret effect has been shown to induce non-trivial effects on the local consumption speed in lean hydrogen-air flames, especially at positive curvature [59]. Although the differences are quantitative, the qualitative behavior remains the same [60–62].

The temperature-based progress variable c used is defined as $c = (T - T_u)/(T_b^\circ - T_u)$, where T_b° is the adiabatic flame temperature. While the actual burned gas temperature of the lean flames may be different from T_b°, considering that the temperature on an iso-mass fraction surface may change even more and that the flame speed depends most strongly on temperature

[58], temperature-based c is adopted as in [47]. It has been ascertained that results with the progress variable based on hydrogen mass fraction (Y_{H_2}), $c_Y = 1 - Y_{H_2}/Y_{H_2,u}$, are qualitatively similar to all the results presented in this paper. Recognizing the caveats presented in [53] due to super-adiabatic temperatures, the analysis is restricted to $c \leq 0.8$.

3. Results and Discussion

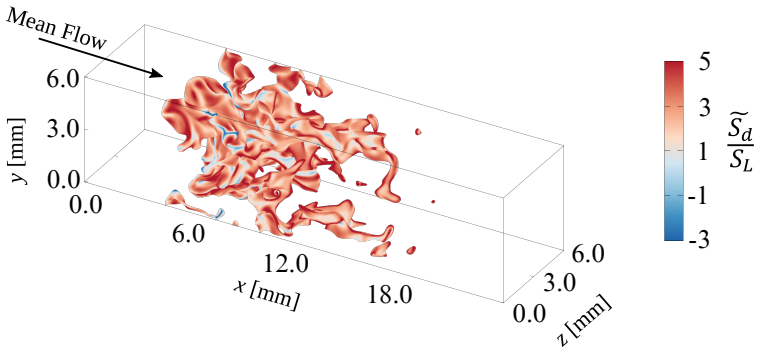

Figure 1: Flame surface ($c_0 = 0.2$) for Le05Ka100 at a given instant of time colored by $\widetilde{S_d}/S_L$.

Figure 1 presents the iso-surface $c = c_0$ where $c_0 = 0.2$ is colored with normalized density-weighted flame displacement speed, $\widetilde{S_d}/S_L = \rho S_d/\rho_u S_L$ at a given time instant for the case Le05Ka100. Qualitatively, an enhancement in $\widetilde{S_d}$ up to a factor of five over S_L is observed at the large negatively curved trailing edge of the flame surface due to flame-flame interaction. Le05Ka100 shows $\widetilde{S_d}/S_L > 1$ for most parts of the iso-scalar surface, in contrast to cases with $Le \approx 1$ discussed in the literature [34, 35] for which most of the regions on the flame surface have $\widetilde{S_d} \approx S_L$.

The widespread enhancement of average $\widetilde{S_d}$ over S_L for Le05Ka100 is also evident from Fig. 2, which presents the joint probability density function (JPDF) of normalized density-weighted local flame displacement speed, $\widetilde{S_d}/S_L$ and the non-dimensional curvature, $\kappa\delta_L$ for Le05Ka100 at $c_0 = 0.05$, 0.2, 0.4 and 0.6 over multiple time instances. The blue curve shows the normalized conditional mean of the density-weighted local flame displacement

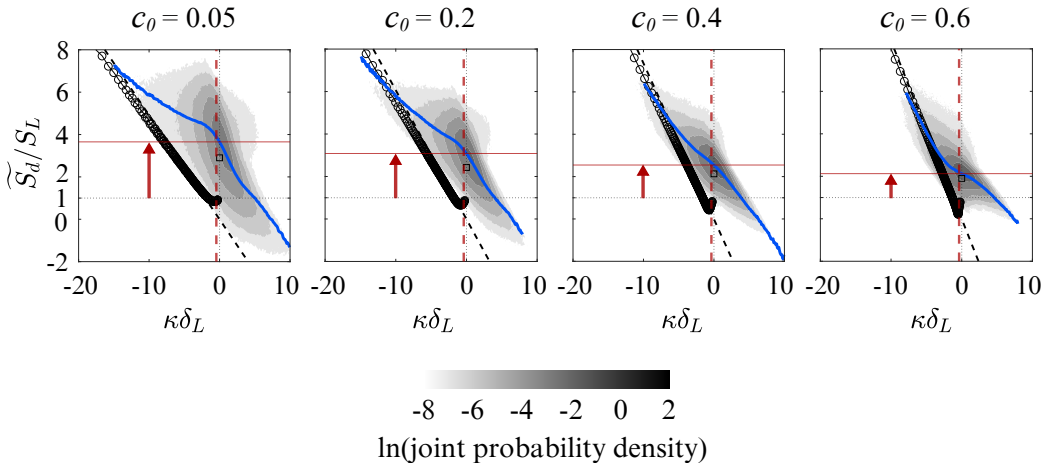

Figure 2: Joint probability density function (JPDF) of normalized density-weighted flame displacement speed, $\widetilde{S_d}/S_L$, and normalized curvature, $\kappa\delta_L$, for iso-scalar, $c_0 = 0.05, 0.2, 0.4$ and 0.6 for Le05Ka100. The colorscale represents the natural logarithm of the JPDF magnitude. The solid blue curve is the conditional mean, $\langle\widetilde{S_d}|_\kappa\rangle/S_L$, at a given κ, obtained from the DNS. The solid horizontal and the dashed vertical red lines show $\widetilde{S_{d,0}}/S_L$ and $\langle\kappa\delta_L\rangle$, respectively. In this paper, we calculate the mean of the variables conditioned on $\kappa = 0$ over a narrow range $-0.1 < \kappa\delta_L < 0.1$. The dashed black line represents the analytical model, $\widetilde{S_d} = -2\widetilde{\alpha_0}\kappa$ and the solid black curve with circular markers represent the IPF results. The hollow square symbol marks $\widetilde{S_{d,0}}/S_L$ conditioned on zero tangential strain rate, $\widetilde{S_{d,0}}|_{a_T=0}/S_L$.

speed at a given curvature $\langle\widetilde{S}_d|_\kappa\rangle/S_L$. Henceforth, $\langle\cdot\rangle$ denotes the mean of the quantity over all the points lying on an iso-surfaces defined by c_0. The mean of the variables conditioned on zero-curvature is calculated over a narrow range $-0.1 < \kappa\delta_L < 0.1$ throughout the present study. The vertical dotted red lines denote the mean non-dimensional curvature $\langle\kappa\delta_L\rangle$ and indicate that $\langle\kappa\delta_L\rangle \approx 0$ for all c_0. Figure 2 overlays the IPF simulation results in solid black lines with black circular symbols, and the corresponding analytical model Eq. (1) in dashed black line, where $\widetilde{\alpha_0}$ is the density-weighted thermal diffusivity computed using Chemkin-PREMIX [63]. The horizontal dotted black line denotes the normalized standard laminar value $\widetilde{S}_d/S_L = 1$. The individual JPDFs also include a hollow square marker in black, which shows the mean of $\widetilde{S}_d|_{\kappa=0}/S_L$ conditioned on zero mean tangential strain rate. This is discussed later in the paper.

The two notably overarching observations from Fig. 2 are the following: (1) The conditional mean of the JPDF (blue curve) asymptotically matches with the IPF simulation as well as the analytical model prediction for $\kappa\delta_L \ll -1$ for all c_0. In fact, with the increase in c_0, the conditional mean aligns perfectly with the IPF and the model. The slope of $\langle \widetilde{S}_d|_\kappa \rangle / S_L$ in the asymptotic limit appears to increase with c_0, consistent with the IPF and model prediction. The increase in slope is mainly due to the increasing density-weighted thermal diffusivity, $\widetilde{\alpha_0}$ in the model. (2) The horizontal solid red line indicate $\widetilde{S_{d,0}}/S_L = \langle \widetilde{S}_d|_{\kappa=0} \rangle / S_L$, whereas the red arrow indicate the net enhancement of $\widetilde{S_{d,0}}/S_L$ over unity. The $\widetilde{S_{d,0}}$ is enhanced to around four times S_L for $c_0 = 0.05$. This deviation of $\widetilde{S_{d,0}}$ from S_L decreases with c_0 as we move further into the flame structure. This observation is in contrast with higher $Le \approx 0.7 - 1.0$ cases [22, 34, 35, 64], where $\widetilde{S_{d,0}} \approx S_L$ for most c_0 values [34], but similar to the observation in [65]. The significance of $\widetilde{S_{d,0}}$ lies in the fact that, on average, the flame surfaces have near zero-curvature (as shown by the dashed vertical red line) and hence in-depth understanding of this deviation of $\widetilde{S_{d,0}}$ from S_L is required.

In the following short subsections, we further elaborate on observation 1, while sections 3.2 and 3.3 will be devoted to investigating observation 2.

3.1. Behavior of $\widetilde{S}_d$ during flame-flame interaction at $\kappa\delta_L \ll -1$

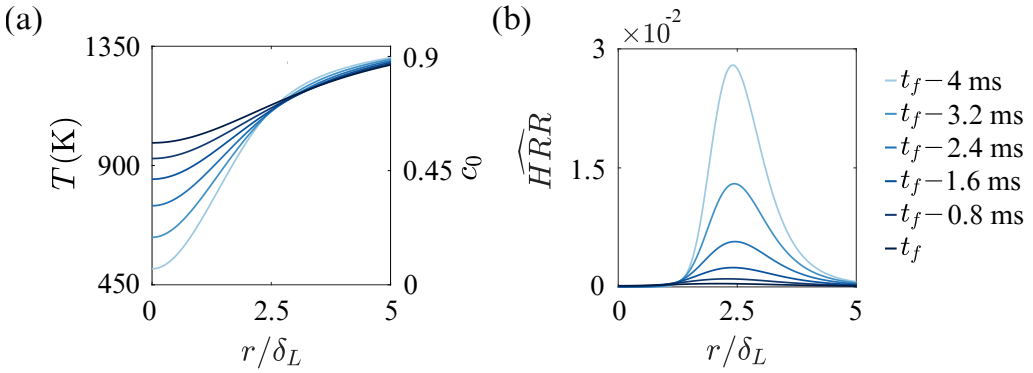

Figure 3: Radial temperature and normalized heat release rate profiles obtained from IPF for conditions as that of Le05Ka100 at various time instances during flame-flame interaction until the iso-scalar $c_0 = 0.6$ is annihilated.

To explain the behavior of $\widetilde{S}_d$ at large negative curvature, $\kappa\delta_L \ll -1$, Fig. 3

shows the temporal evolution of temperature and the heat release rate (HRR) profiles obtained from the IPF simulation at the thermodynamic conditions of Le05Ka100 during the annihilation event. The HRR is normalized by its maximum standard laminar value. Note that the HRR barely exist with 3% of the laminar value even before the onset of interaction due to strong negative stretch rates and Le effects. As the preheat zone flame-flame interaction proceeds, the HRR eventually becomes zero. Thus the heat release zone never interacts. This is in compliance with the inherent assumption of non-interacting heat release layers of the interacting flame theory describing the local cylindrical self-interaction among the isotherms in turbulent flames at large negative κ resulting in enhanced $\widetilde{S}_d$ [22, 34] even for ultra-lean hydrogen flames. This results in a near-perfect agreement between the theoretical model (Eq. 1) and the DNS results for the ultra-lean hydrogen-air flame at very large negative curvatures.

3.2. Can $\widetilde{S}_d$ at $\kappa\delta_L = 0$ be described using counterflow flames?

A 1D cylindrical flame model successfully explained the limiting behavior of $\widetilde{S}_d$ at large negative κ for locally interacting premixed flames in turbulence. It is well known that the material or propagating surfaces undergo straining in turbulence [36, 66–68]. Hence, we use a planar flame with finite tangential strain rate to understand the large increase in $\widetilde{S_{d,0}}/S_L$ as found from DNS at $\kappa\delta_L \approx 0$. In the following sub-section, results from the second model configuration of a 1D premixed counterflow flame (CFF) [69–72], with the tangential strain rate, $a_{T,CFF}$ representing the mean value over the iso-scalar surface for the DNS data at $\kappa = 0$, i.e. $\langle a_T|_{\kappa=0}\rangle$ (a_T being tangential strain rate from DNS), is considered as an attempt to explain the deviation of $\widetilde{S_{d,0}}$ from S_L. For consistency in nomenclature, we define $a_{T,0} = \langle a_T|_{\kappa=0}\rangle$, whereas the subscript CFF is used for counterflow flame. The results from CFF are compared with those obtained from the DNS for all the cases at iso-tangential strain rate, i.e., $a_{T,CFF} = a_{T,0}$. While, the present subsection discusses the key findings and the shortcomings of the canonical form in describing the behavior of $\widetilde{S_{d,0}}$ the following subsection explores the underlying reasons for the same.

Figure 4 presents the joint probability density function (JPDF) of normalized density-weighted flame displacement speed and tangential strain rate conditioned on zero-curvature locations for Le05Ka100 at $c_0 = 0.05, 0.2, 0.4$ and 0.6. Each of the JPDF is superimposed with $\langle \widetilde{S}_d|_{\kappa=0,a_T}\rangle/S_L$, i.e., the conditional mean of $\widetilde{S}_d/S_L$ given a_T, at zero-curvature shown in blue curve.

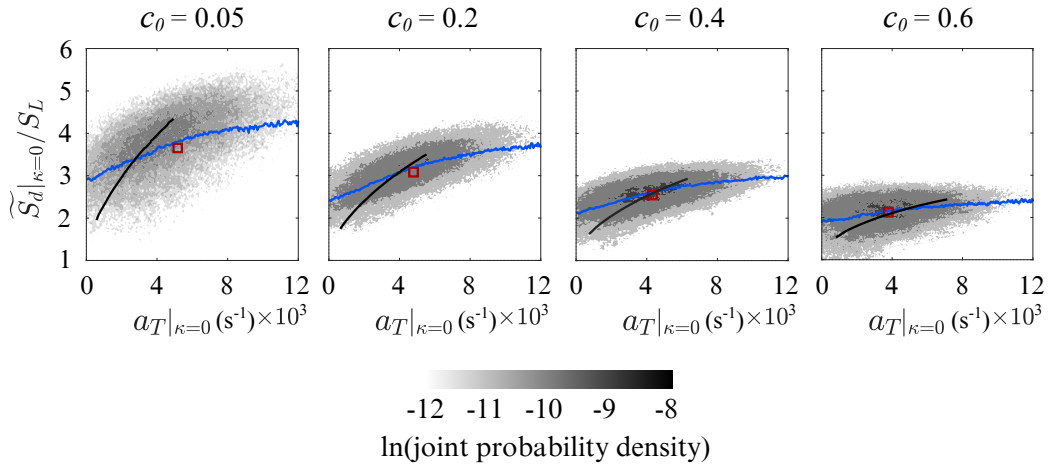

Figure 4: Joint probability density function (JPDF) of $\widetilde{S_d}|_{\kappa=0}/S_L$ and $a_T|_{\kappa=0}$ for Le05Ka100 at c_0 = 0.05, 0.2, 0.4 and 0.6. The colorscale corresponds to the natural logarithm of the joint probability density magnitude. The conditional mean of normalized density-weighted local flame displacement speed at zero-curvature given tangential strain, $\langle\widetilde{S_d}|_{\kappa=0,a_T}\rangle/S_L$ is presented by the blue curve. The hollow red square represents the point ($a_{T,0}$, $\widetilde{S_{d,0}}/S_L$). The solid black curves represent the corresponding CFF solution.

The hollow square marker in red represents the point ($a_{T,0}$, $\widetilde{S_{d,0}}/S_L$). The CFF solutions at the same c_0 (T_0) are represented in black curves. Although the nature of the overall response of $\langle\widetilde{S_d}|_{\kappa=0,a_T}\rangle/S_L$ to tangential strain rate $a_T|_{\kappa=0}$ is qualitatively similar to that given by CFF [73] the strain response of the flame in turbulence is much weaker than that in the CFF configuration. Interestingly, while the CFF solution approaches S_L at zero tangential strain rate, $\langle\widetilde{S_d}|_{\kappa=0,a_T=0}\rangle > S_L$ (see Fig. 2) for all isotherms under investigation. At $a_{T,CFF} = a_{T,0}$ it is seen that CFF fails to predict the mean DNS trends at higher $a_{T,0}$ or lower c_0 (c_0 = 0.05, 0.2) but at c_0 = 0.4, 0.6 the CFF results are fairly close to that of $\widetilde{S_{d,0}}/S_L$. The variation of $\widetilde{S_{d,0}}/S_L$ with $a_{T,0}$ for Le05Ka100 are shown in Fig. 5a in hollow markers. The CFF solutions at c_0 = 0.05, 0.2, 0.4 and 0.6 from Fig. 4 for the corresponding c_0 are also included. Fig. 5b and c present similar plots for Le08Ka1000 and Le1Ka100, respectively. The colorscale at the bottom represents the c_0 for both DNS and CFF simulations.

Comparing the DNS and the CFF results in the preheat zone before maximum heat release rate for Le05Ka100 (all the four c_0 values) and Le1Ka100

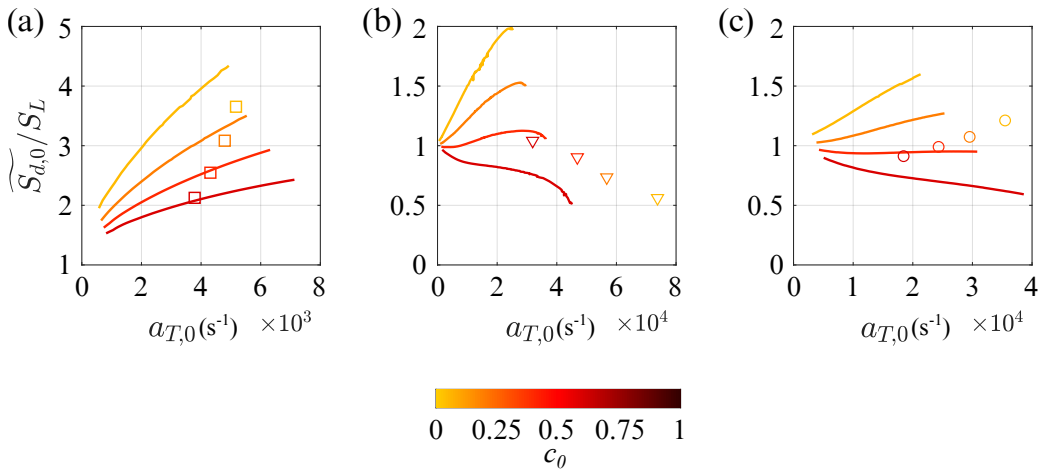

Figure 5: The variation of $\widetilde{S_{d,0}}/S_L$ with $a_{T,0}$ for (a) Le05Ka100 (b) Le08Ka1000 (c) Le1Ka100 in hollow markers. The solid lines represent the results from CFF. The colorscale corresponds to c_0.

(c_0 = 0.05 and 0.2) show that indeed $\widetilde{S_{d,0}}$ increases beyond S_L under positive tangential straining, but their mutual agreement is inconsistent. CFF fails to provide any solution at c_0 = 0.05 for Le05Ka100 and c_0 = 0.05, 0.2 for Le1Ka100 at equal tangential strain rate conditions. Furthermore, even if a solution exists, it is larger than $\widetilde{S_{d,0}}$ obtained from DNS for c_0 before the maximum heat release rate. While for c_0 post maximum heat release rate the CFF solutions are smaller than $\widetilde{S_{d,0}}$, i.e., c_0 = 0.4, 0.6 for Le1Ka100. Thus, the trends of $\widetilde{S}_d|_{\kappa=0}$ with $a_T|_{\kappa=0}$, as well as their corresponding mean, are quantitatively different from the CFF solutions for Le05Ka100 and Le1Ka100. While the CFF trends remain the same for Le08Ka100, the trends in DNS results are different. Consistency persists in the fact that at c_0 = 0.6 (beyond maximum heat release rate), the CFF solution is lower than the DNS result while no solutions are found at lower c_0. It is inferred that under the same tangential strain rate, CFF is unable to describe the mean local flame structure at κ = 0 in 3D turbulent flames. Thus, the canonical configuration falls short in describing the behavior of $\widetilde{S_{d,0}}$. This is consistent with [72], where the local structure of leading regions was compared with those from critically strained flames. This was attributed to history or transient effects for turbulent flames by Im et al. [74], as such conditioning on a_T = 0 also

yields $\widetilde{S_{d,0}}|_{a_T=0} > S_L$ for Le05Ka100 case as shown using black squares in Fig. 2 in agreement with [65]. Hence, further investigation of $\widetilde{S_{d,0}}$ is necessary based on the mean local flame structure, the effect of which on S_d will be instantaneous, eliminating history effects.

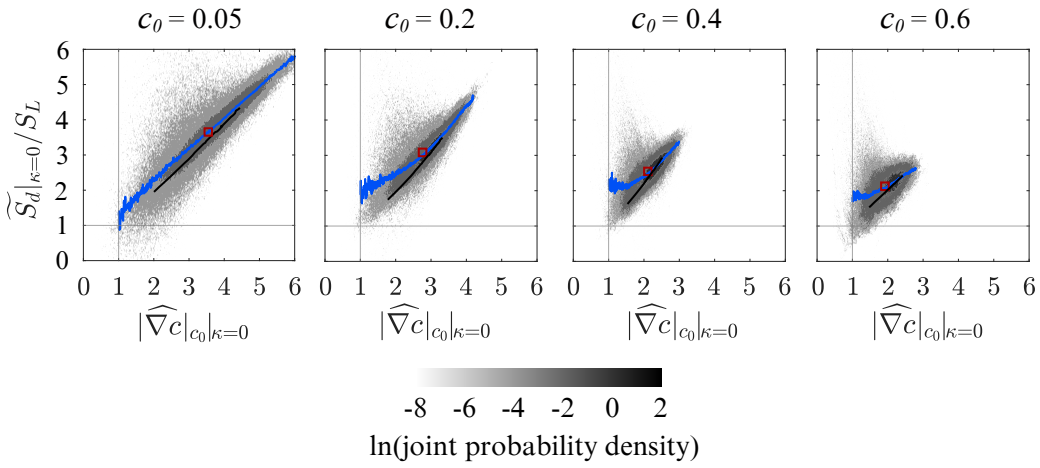

Figure 6: Joint probability density function (JPDF) of $\widetilde{S_d}|_{\kappa=0}/S_L$ with $|\widehat{\nabla c}|_{c_0}|_{\kappa=0}$ for Le05Ka100 at c_0 = 0.05, 0.2, 0.4 and 0.6. The colorscale corresponds to the natural logarithm of the joint probability density magnitude. The conditional mean given normalized scalar gradient conditioned on zero-curvature, $\langle \widetilde{S_d}|_{\kappa=0,|\widehat{\nabla c}|_{c_0}|_{\kappa=0}} \rangle$ is presented by the blue curve. The hollow square red markers represent the point ($\langle |\widehat{\nabla c}|_{c_0}|_{\kappa=0} \rangle$, $\widetilde{S_{d,0}}/S_L$). The solid black curves represent the CFF solution.

Previously, the magnitude of the scalar gradient $|\nabla c|$ has been used as a measure of separation between the iso-scalar surfaces [38, 75]. In fact, the inverse of the local scalar gradient magnitude has been defined as the local flame width [75]. Hence, it is first recognized that the magnitude of the scalar gradient of the progress variable normalized by the corresponding laminar value at that c_0, $|\nabla c|_{c_0}/|\nabla c|_{c_0,L}$, is a possible measure of the local flame structure compared to its standard laminar counterpart. Thus we seek to correlate $\widetilde{S_d}|_{\kappa=0}/S_L$ and the normalized absolute gradient of the progress variable conditioned on κ = 0, $|\widehat{\nabla c}|_{c_0}|_{\kappa=0} = |\nabla c|_{c_0}|_{\kappa=0}/|\nabla c|_{c_0,L}$. Figure 6 shows the joint probability density function of $\widetilde{S_d}|_{\kappa=0}/S_L$ and $|\widehat{\nabla c}|_{c_0}|_{\kappa=0}$ for the case Le05Ka100 at the four c_0 values superimposed with the conditional mean of $\widetilde{S_d}|_{\kappa=0}/S_L$ given $|\widehat{\nabla c}|_{c_0}|_{\kappa=0}$. The corresponding CFF solutions are shown in

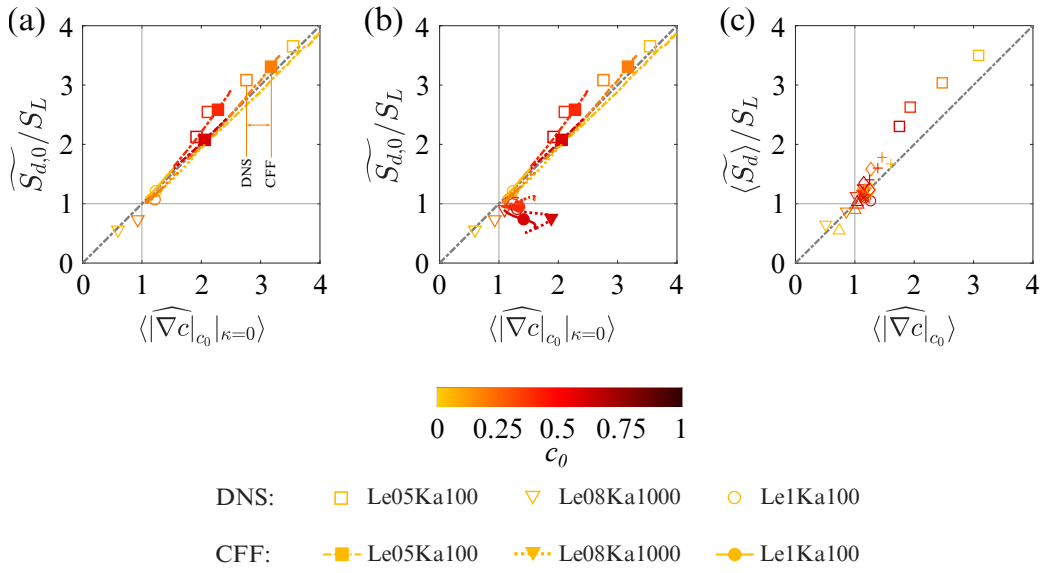

Figure 7: Correlation of $\widetilde{S_{d,0}}/S_L$ with $\langle|\widehat{\nabla c}|_{c_0}|_{\kappa=0}\rangle$ for DNS and laminar CFF (a) in the preheat zone (c_0 before maximum heat release rate only) (b) over the entire flame structure at $c_0 = 0.05, 0.2, 0.4$ and 0.6. Hollow symbols represent DNS data, and filled symbols of the same shape represent CFF data at the same thermodynamic conditions, with $a_{T,CFF} = a_{T,0}$. Lines show CFF solutions over varying $a_{T,CFF}$. (c) Correlation of $\langle\widetilde{S_d}\rangle/S_L$ with $\langle|\widehat{\nabla c}|_{c_0}|\rangle$ for the present cases and those from previous studies [34, 35, 43]. Data from these additional cases are denoted by: F1: '☆', F3: '×', F4: '△', P3: '◊', P7: '+'

the solid black curve. It is apparent that $\widetilde{S_d}|_{\kappa=0}/S_L$ correlate fairly well with $|\widehat{\nabla c}|_{c_0}|_{\kappa=0}$ for both the DNS as well as the CFF. The conditional mean from DNS closely follows the CFF solution at $c_0 = 0.05$ and 0.2. At $c_0 = 0.4$ and 0.6 the average slope of the conditional mean shows deviation from unity. Nevertheless, the point $(\langle|\widehat{\nabla c}|_{c_0}|_{\kappa=0}\rangle,\ \widetilde{S_{d,0}}/S_L)$ shown in hollow red square lie close to the CFF solution for all c_0. Next, we proceed to correlate the averages: $\widetilde{S_{d,0}}/S_L$ and $\langle|\widehat{\nabla c}|_{c_0}|_{\kappa=0}\rangle$ from DNS as well as from CFF in Fig. 7. The figure shows the results for the three DNS cases under study as well as cases F1, F4, P3 and P7 from previous studies [34, 35, 43] for a wider range of Ka, Re_t and Le conditions. The results from CFF simulations with varying $a_{T,CFF}$ for $c_0 = 0.05, 0.2, 0.4$ and 0.6 are shown in different line types, whereas the solid markers correspond to CFF solutions at $a_{T,CFF} = a_{T,0}$ conditioned on the same isotherms. The dash-dotted grey line denoting Eq. (5) with

unity slope is obtained from an approximate scaling analysis of Eq. (4) for $\kappa = 0$ (see Appendix A).

$$\frac{\widetilde{S}_d|_{\kappa=0}}{S_{L_{c,0}}} \approx \frac{|\nabla c|_{c_0}|_{\kappa=0}}{|\nabla c|_{c_0,L}} = |\widehat{\nabla c}|_{c_0}|_{\kappa=0} \tag{5}$$

Figure 7a includes the points for c_0 before the maximum heat release rate and Fig. 7b at all c_0 values. Overall, $\widetilde{S_{d,0}}/S_L$ show a good correlation with $\langle|\widehat{\nabla c}|_{c_0}|_{\kappa=0}\rangle$ for all the DNS cases and CFF solutions in the preheat zone. This observation is consistent with that in [34], but generalizes the findings to a much wider range of Le conditions over large $\langle|\widehat{\nabla c}|_{c_0}|_{\kappa=0}\rangle$ values. Overall, Eq. (5) qualitatively justifies the above observations. Figure 7c shows that $\langle\widetilde{S}_d\rangle/S_L$ and $\langle|\widehat{\nabla c}|_{c_0}\rangle$ are also very well correlated since for all the surfaces $\langle\kappa\delta_L\rangle \approx 0$ (see Fig. 2). Nevertheless, from the data it is apparent that Le05Ka100 case exhibits more thinned preheat zones with increased $\langle|\widehat{\nabla c}|_{c_0}|_{\kappa=0}\rangle$, resulting in large $\widetilde{S_{d,0}}/S_L$, while Le08Ka1000 and Le1Ka100 cases show local broadening in preheat zone thickness with $\widetilde{S_{d,0}}/S_L < 1$. While the suggested correlations show overall good agreement for all Le conditions under study, there is an additional important issue that needs further discussion. The data points from CFF calculations at $a_{T,CFF} = a_{T,0}$ (shown in filled symbols) for the Le05Ka100 case, appear at higher values along both axes when compared to the DNS in Fig. 7a (shown in hollow symbols but of the same shape). This implies that the turbulent flame segment with zero-curvature subjected to the same average tangential strain rate has a relatively smaller net flame thinning effect compared to the steady laminar strained flame counterpart. It seems that there is some degree of attenuation in the effect of local straining of the turbulent flame. In other words, the flame surface is locally thinned or propagates faster on average compared to the standard laminar flame, while thickened or propagates slower compared to the corresponding CFF. For the cases, Le08Ka1000 and Le1Ka100, the net broadening of the flame structure is observed. One may argue that this broadening is due to turbulence mitigating the local flame surface's response to the local tangential strain rate, reducing $\widetilde{S_{d,0}}$ relative to the CFF $\widetilde{S}_d$ values at $a_{T,CFF} = a_{T,0}$. However, it cannot be concluded that for a premixed flame with even lower Le and Ka, $\widetilde{S_{d,0}}$ cannot be higher than the corresponding CFF solution. This is discussed later in section 3.3.2. However, based on the DNS cases currently investigated, we observe a consistent effect residing in turbulence-flame interaction where the turbulent flames are broadened on

average compared to equivalent laminar strained flames.

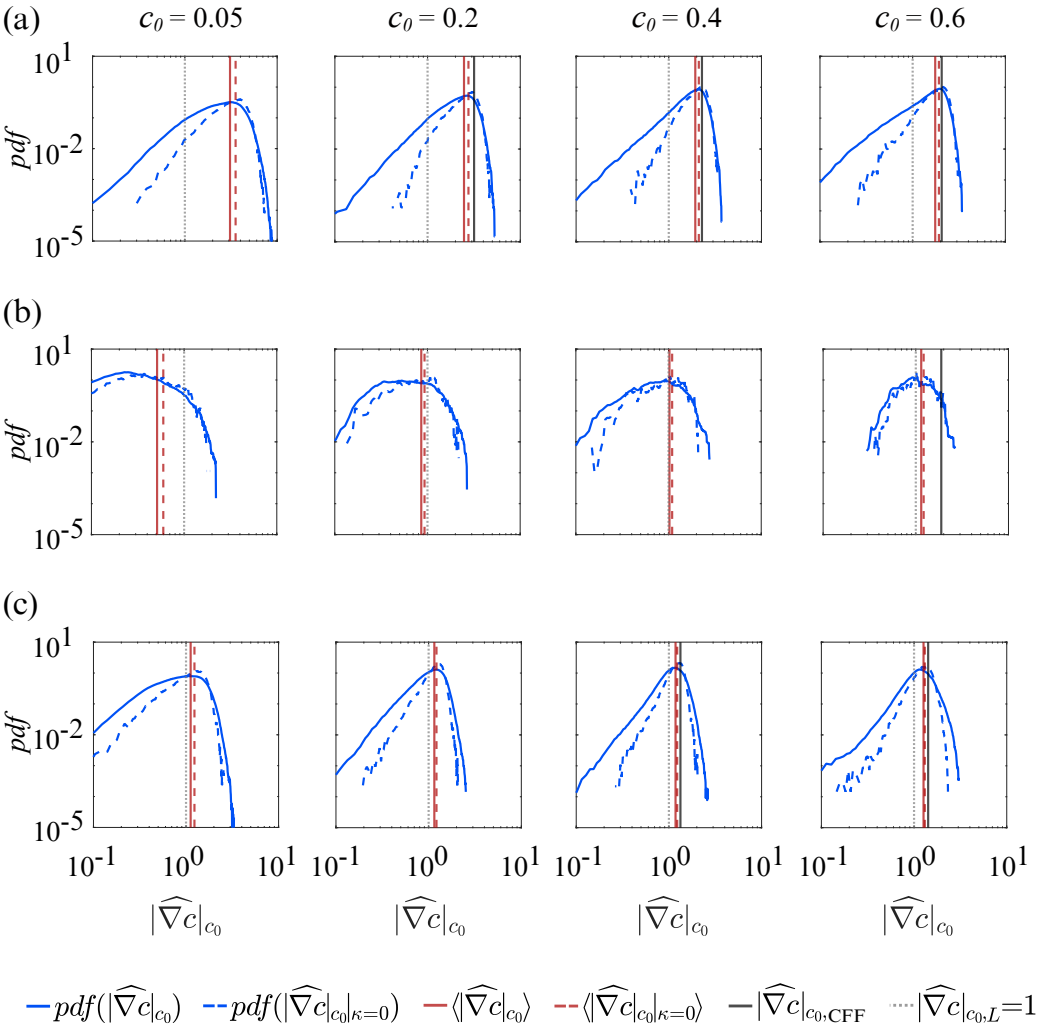

Figure 8: Probability density function (PDF) of $|\widehat{\nabla c}|_{c_0}$ (solid blue curve) and $|\widehat{\nabla c}|_{c_0}|_{\kappa=0}$ (dashed blue curve) at $c_0 = 0.05, 0.2, 0.4$ and 0.6 for (a) Le05Ka100 (b) Le08Ka1000 (c) Le1Ka100. The solid and dashed vertical red line denote their respective means, $\langle|\widehat{\nabla c}|_{c_0}\rangle$ and $\langle|\widehat{\nabla c}|_{c_0}|_{\kappa=0}\rangle$. The solid black lines represent the CFF solution, whereas the dotted gray line denotes the standard laminar value, $|\widehat{\nabla c}|_{c_0,L} = 1$.

As a further proof, the probability density function (PDF) of $|\widehat{\nabla c}|_{c_0}$ and $|\widehat{\nabla c}|_{c_0}|_{\kappa=0}$ is shown in Fig. 8 for $c_0 = 0.05, 0.2, 0.4$ and 0.6 for the case (a)

Le05Ka100 (b) Le08Ka1000 (c) Le1Ka100. The pdfs of $|\widehat{\nabla c}|_{c_0}$ and $|\widehat{\nabla c}|_{c_0}|_{\kappa=0}$ are shown in solid and dashed blue curves. The solid and dashed vertical red lines represent their corresponding means. The solid black lines are CFF solutions, whereas the dotted gray line denotes the standard laminar value, i.e., $|\widehat{\nabla c}|_{c_0,L} = 1$. The pdfs ($|\widehat{\nabla c}|_{c_0}$ and $|\widehat{\nabla c}|_{c_0}|_{\kappa=0}$) appear quasi log-normal but with a distinctive negative skewness. The negative skewness in the pdf of $|\widehat{\nabla c}|_{c_0}$ was also observed by [38, 47]. The negative skewness or occurrence of such small values of $|\widehat{\nabla c}|_{c_0}$ is attributed to the regions on the flame surfaces undergoing flame-flame interactions at large negative curvature ($\kappa\delta_L \ll -1$) leading to homogenization of gradients ($|\widehat{\nabla c}|_{c_0} \to 0$). On the other hand, pdf of $|\widehat{\nabla c}|_{c_0}|_{\kappa=0}$ includes the points on the flame surfaces in the non-interacting regime ($\kappa\delta_L \approx 0$) but is still negatively skewed resulting in $|\widehat{\nabla c}|_{c_0}|_{\kappa=0} < |\widehat{\nabla c}|_{c_0,CFF}$. The existence of such low $|\widehat{\nabla c}|_{c_0}|_{\kappa=0}$ needs investigation. Overall, on average, the flame for Le05Ka100 and Le1Ka100 for most parts is thinned w.r.t. the standard laminar flame but is thickened w.r.t. the CFF flame structure. However, in Le08Ka1000 the flame is thickened for most parts w.r.t. the standard laminar flame except at large c_0 values.

3.3. Non-local effects influencing $\widetilde{S}_d$ at $\kappa\delta_L = 0$

3.3.1. Non-local effect of flame-flame interaction at large negative curvatures on $\widetilde{S}_d$ at $\kappa\delta_L = 0$

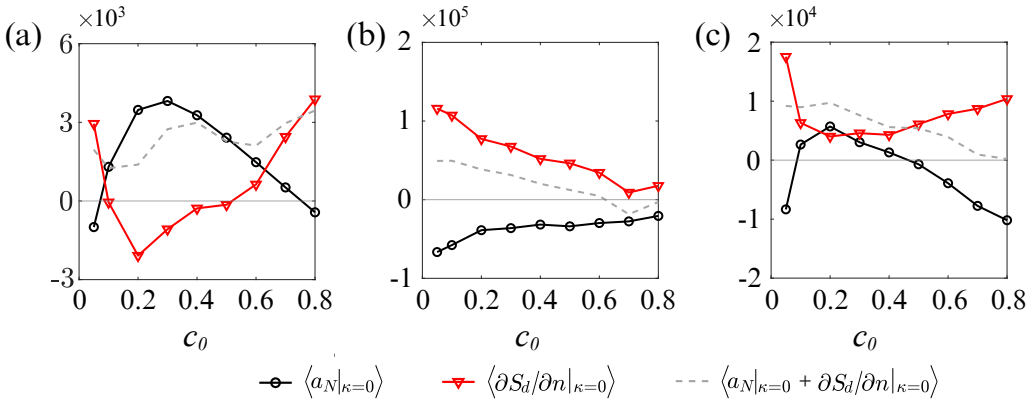

Figure 9: Variation of mean of normal strain rate (a_N) and $\partial S_d/\partial n$ conditioned on $\kappa = 0$ with c_0 for (a) Le05Ka100 (b) Le08Ka1000 (c) Le1Ka100. The dashed gray curve denotes the sum of the two terms.

Since $\widetilde{S_{d,0}}$ and $\langle|\widehat{\nabla c}|_{c_0}|_{\kappa=0}\rangle$ were found to be well correlated, we seek to understand the deviation of $|\widehat{\nabla c}|_{c_0}|_{\kappa=0}$ from its corresponding CFF as well as the standard laminar value. To that end, we consider the transport equation for $|\widehat{\nabla c}|$ in the Lagrangian form at the flame surface [47, 76–78]:

$$\frac{\widetilde{D}|\widehat{\nabla c}|}{\widetilde{D}t} = -\left[a_N + \frac{\partial S_d}{\partial n}\right]|\widehat{\nabla c}| \tag{6}$$

where a_N is the fluid motion-induced normal strain rate and $\partial S_d/\partial n$ is the normal strain rate due to flame propagation with the normal, $\boldsymbol{n} = -\nabla c/|\nabla c|$ being the local normal in the direction of the reactants. Each term on the right-hand side shows the mechanism of thickening or thinning of the flame structure. In steady flames, the sum is identically zero. Fig. 9 shows the variation of the mean a_N and $\partial S_d/\partial n$ conditioned on $\kappa = 0$ with c_0 for all the cases. Dopazo et al. [77] reported $\langle a_N\rangle > 0$ and $\langle\partial S_d/\partial n\rangle < 0$ for low Ka flames. In the present study, we found that for Le08Ka1000 and Le1Ka100, $\langle\partial S_d/\partial n|_{\kappa=0}\rangle > 0$, similar to those observed in large Ka methane-air Bunsen flames by Wang et al. [78] but in direct contrast to planar laminar unstrained/strained flame behavior where $\partial S_d/\partial n = -a_N < 0$. Although Le05Ka100 shows $\langle\partial S_d/\partial n|_{\kappa=0}\rangle < 0$ for $0.1 < c_0 < 0.5$ its magnitude is much less than $\langle a_N|_{\kappa=0}\rangle$. For $Ka \sim 100$ cases, $\langle a_N|_{\kappa=0}\rangle > 0$ possibly due to dilatation, while for $Ka \sim 1000$, $\langle a_N|_{\kappa=0}\rangle < 0$. The nature of $\langle a_N|_{\kappa=0}\rangle$ in turbulent premixed flame based on the alignment of the smallest principal strain rate and the normal to the iso-scalar surfaces have been discussed [47, 79]. Unlike a steady laminar flame, where positive a_N and negative $\partial S_d/\partial n$ balance out, in these turbulent flames, their net contribution remains positive (dashed gray curve). This is primarily due to $\langle\partial S_d/\partial n|_{\kappa=0}\rangle$ attaining positive values or small negative values that are insufficient to balance $\langle a_N|_{\kappa=0}\rangle$, leading to local flame broadening.

We seek to understand such crucial behavior of the normal gradient of the flame speed, which is central to flame thickening and associated reduction in $\widetilde{S_{d,0}}$. Conditionally averaged flame structures along their local normal directions from surface locations $c = c_0$ where $\kappa = 0$, are analyzed. Figure 10 presents a schematic including the two-dimensional contour of heat release rate overlaid with iso-scalar curves at mid-plane extracted from Le05Ka100 at a given time instant. The schematic includes two points, x_1 and x_2 on a selected iso-scalar surface $c = c_0$ where $\kappa \approx 0$. The local normal at these points extending in either direction is shown in blue. The local flame struc-

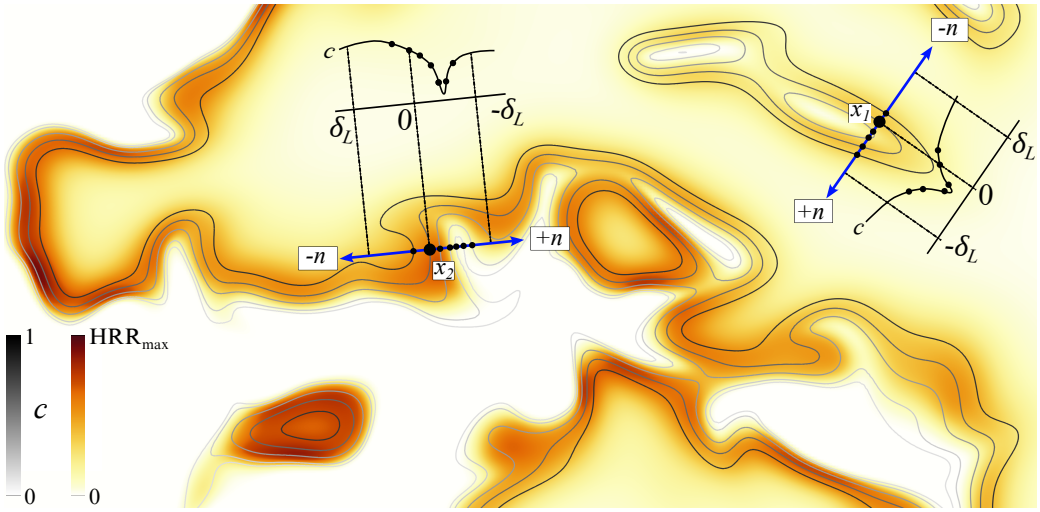

Figure 10: Two-dimensional contour of heat release rate overlaid with iso-scalar curves at mid-plane extracted from Le05Ka100 at a given time instant. x_1 and x_2 are the points on a selected iso-scalar surface $c = c_0$ where $\kappa \approx 0$. The local normal at these points extending in either direction is shown in blue. The local flame structures based on c extracted on either side of x_1 and x_2 along their normal direction up to a distance of δ_L are shown in black. The circular markers on the c profile represent the c values at the corresponding neighboring iso-scalar.

tures are extracted on either side of x_1 and x_2 along their normal direction up to a distance of δ_L. The obtained local flame structures based on c are shown in black, with the circular markers representing the c values at the corresponding neighboring iso-scalar surface. Note that the actual structures are generated from the 3D DNS fields. For further details regarding the algorithm followed, the readers can refer to Yuvraj et al. [34, 35]. Figure 11a shows the mean local flame structure (black for c and red for S_d/S_L) conditioned on $\kappa = 0$ for the flame surfaces $c_0 = 0.05, 0.2, 0.4$ and 0.6 for Le05Ka100. The corresponding flame structures from standard laminar flame are shown in faint curves. The vertical grey line, i.e., $\xi/\delta_L = 0$ is the origin lying on the corresponding c_0 where $\kappa = 0$. The mean c and S_d/S_L values at $\xi/\delta_L = 0$ are represented by black and red square markers, respectively. $\partial S_d/\partial n$ is indeed positive or weakly negative at the points on the flame surface conditioned on $\kappa = 0$ ($\xi/\delta_L = 0$) in the preheat zone in agreement with Fig. 9. This is because such points are preceded by a sharp increase in S_d along $\boldsymbol{n}$ on the

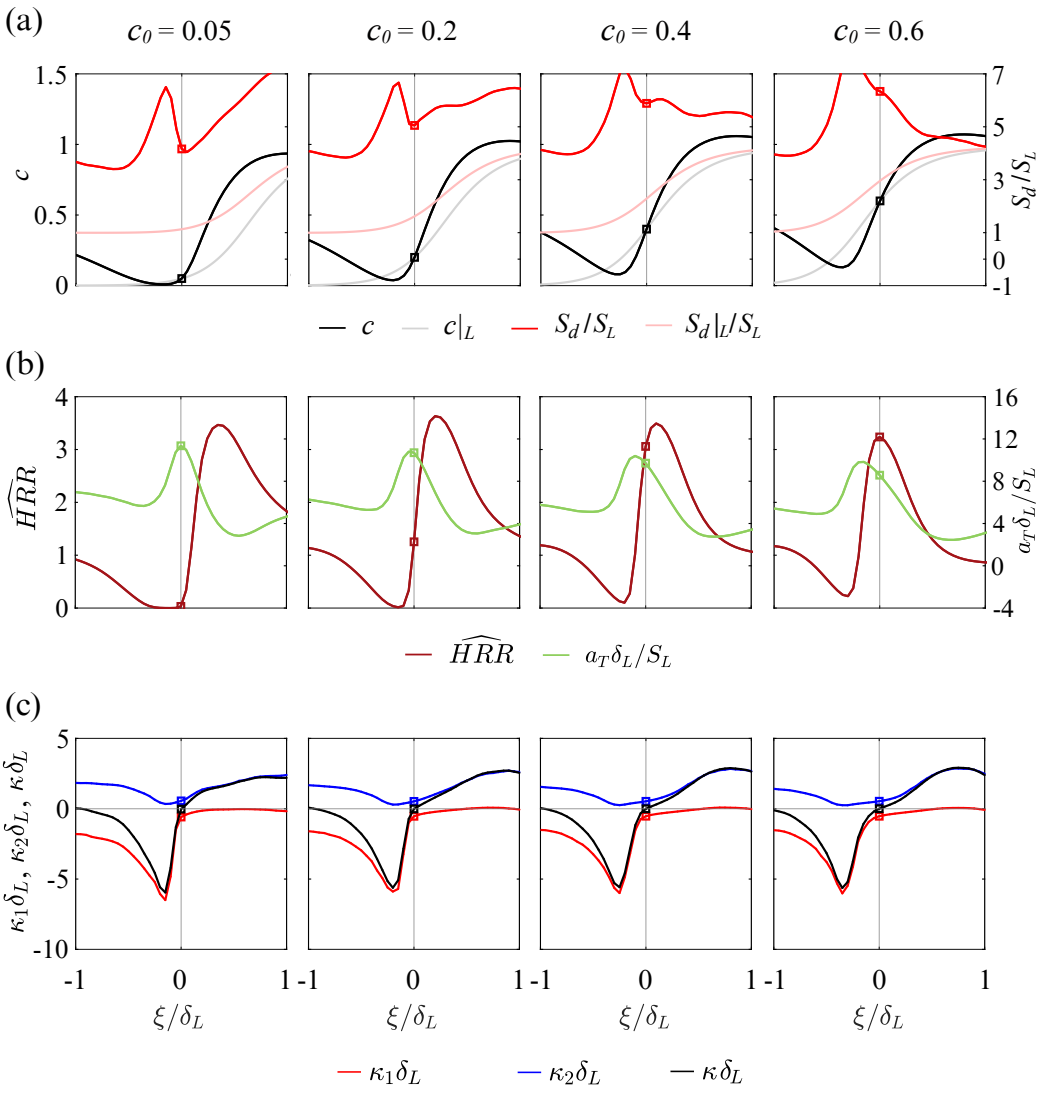

Figure 11: Mean local flame structures of (a) c and S_d/S_L (b) normalized heat release rate, $\widehat{HRR}$ and non-dimensional tangential strain rate, $a_T\delta_L/S_L$ (c) non-dimensional curvature $\kappa\delta_L$, non-dimensional minimum and maximum principal curvatures, $\kappa_1\delta_L$ and $\kappa_2\delta_L$ conditioned on $\kappa = 0$ at $c = c_0$ for Le05Ka100. The faint red and gray curves in the background in (a) represent the corresponding standard laminar flame structures.

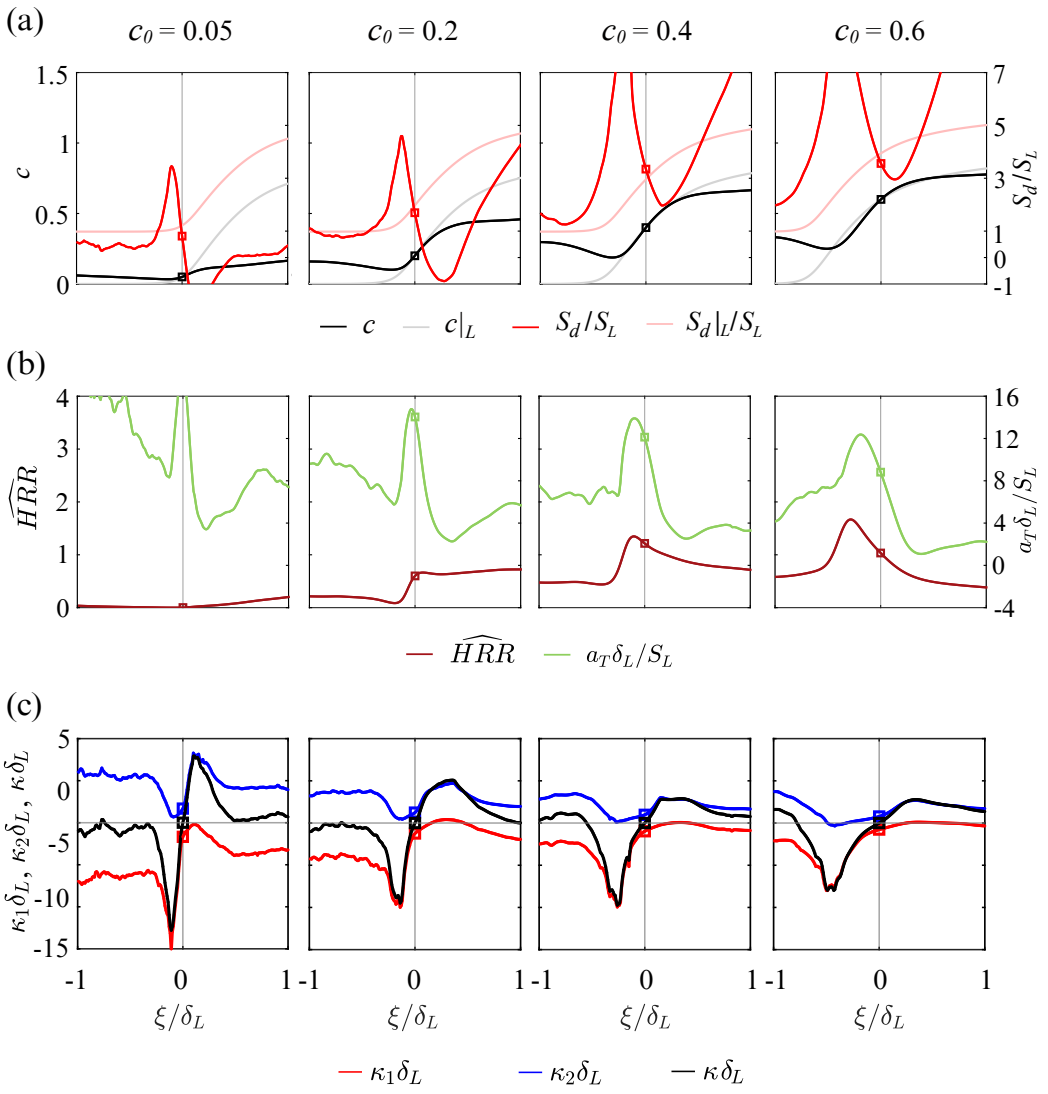

Figure 12: Mean local flame structures of (a) c and S_d/S_L (b) normalized heat release rate, $\widehat{HRR}$ and non-dimensional tangential strain rate, $a_T\delta_L/S_L$ (c) non-dimensional curvature $\kappa\delta_L$, non-dimensional minimum and maximum principal curvatures, $\kappa_1\delta_L$ and $\kappa_2\delta_L$ conditioned on $\kappa = 0$ at $c = c_0$ for Le08Ka1000. The faint red and gray curves in the background in (a) represent the corresponding standard laminar flame structures.

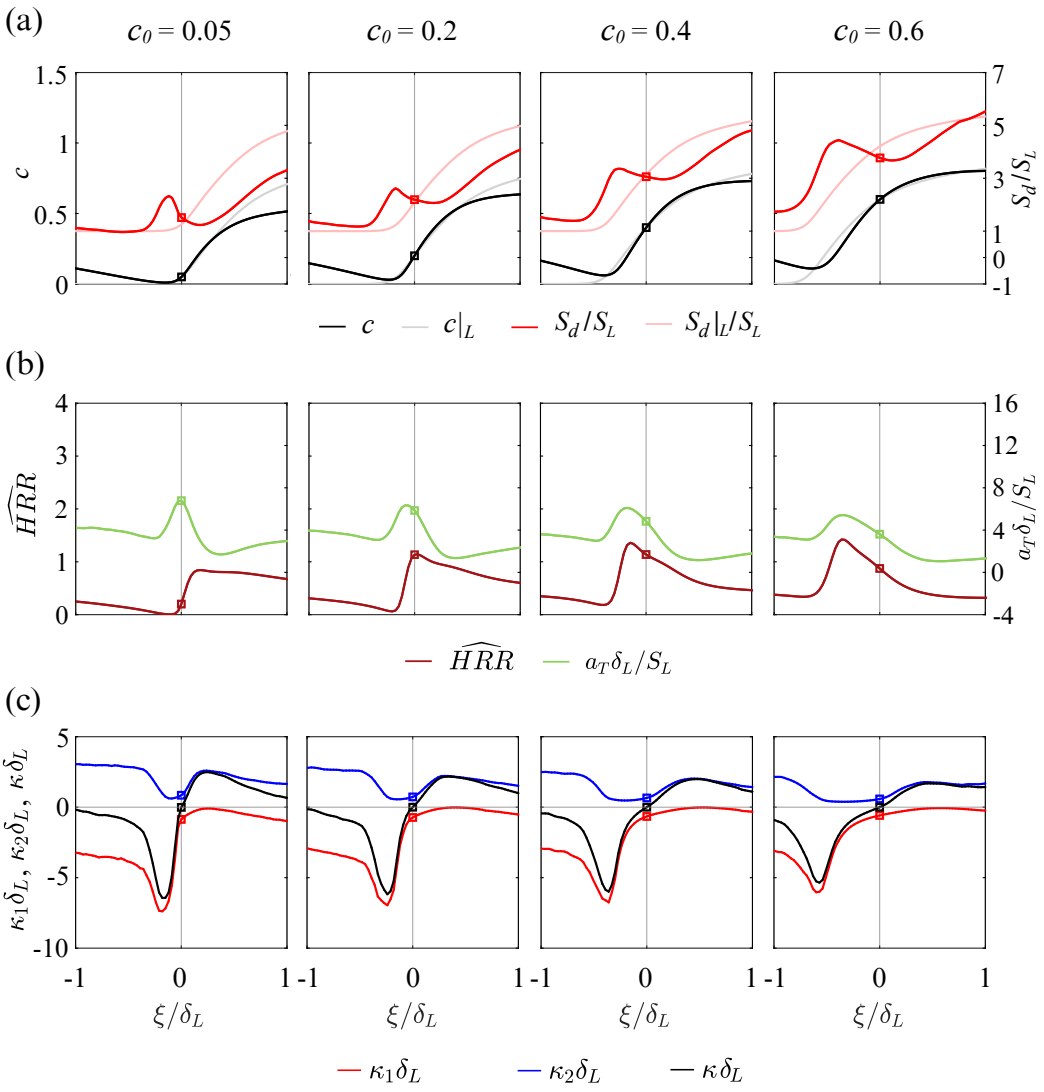

Figure 13: Mean local flame structures of (a) c and S_d/S_L (b) normalized heat release rate, $\widehat{HRR}$ and non-dimensional tangential strain rate, $a_T\delta_L/S_L$ (c) non-dimensional curvature $\kappa\delta_L$, non-dimensional minimum and maximum principal curvatures, $\kappa_1\delta_L$ and $\kappa_2\delta_L$ conditioned on $\kappa = 0$ at $c = c_0$ for Le1Ka100. The faint red and gray curves in the background in (a) represent the corresponding standard laminar flame structures.

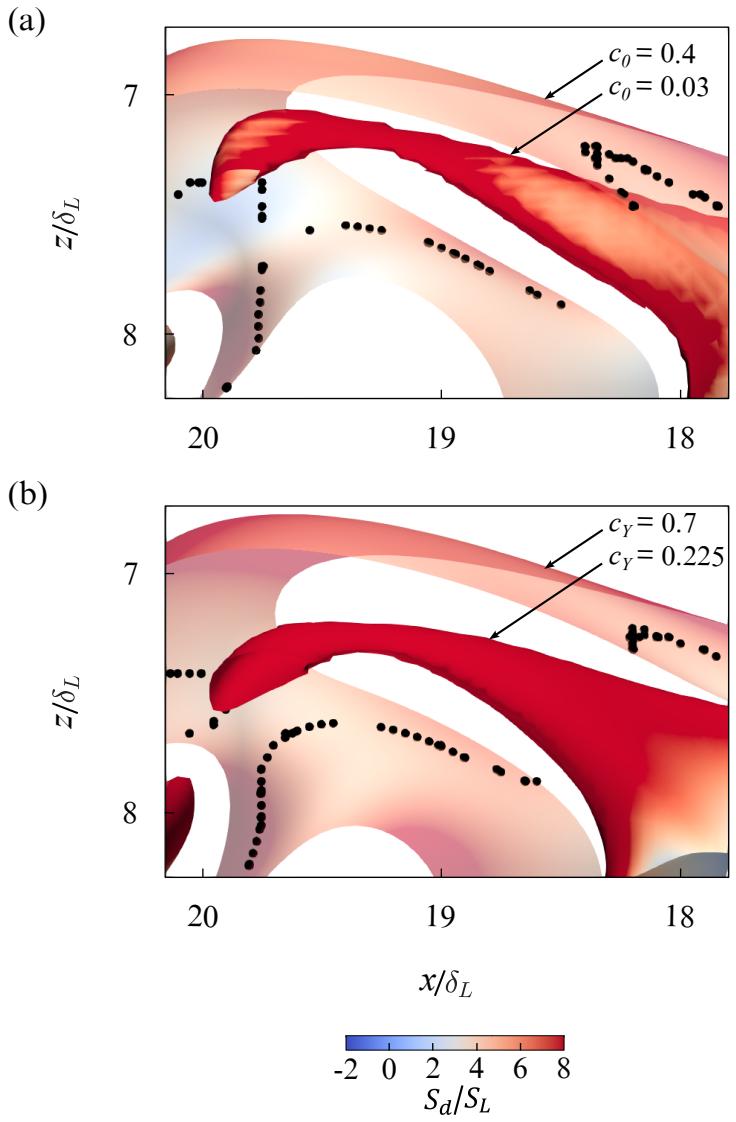

Figure 14: Segments of the iso-scalar surfaces of Le05Ka100 colored by S_d/S_L based on (a) T: $c_0 = 0.03$ and 0.4 (b) Y_{H_2}: $c_Y = 0.225$ and 0.7. The black markers denote the points with $\kappa = 0$ on (a) $c_0 = 0.4$ and (b) $c_Y = 0.7$.

upstream, starkly contrasting with any laminar flame structure (strained or unstrained). The V-shaped average temperature profile suggesting possible flame-flame interaction just preceding the point of interest is also apparent. The second set of flame structures based on the heat release rate normalized by the corresponding maximum laminar value (shown in dark red) and non-dimensional tangential strain rate, $a_T\delta_L/S_L$ (shown in green) is included in Fig. 11b.

Finally, Fig. 11c presents the third set of conditionally averaged local flame structures (from $c = c_0$ and $\kappa = 0$) along $\boldsymbol{n}$ which includes non-dimensional total curvature, $\kappa\delta_L$ in black, minimum and maximum non-dimensional principal curvatures, $\kappa_1\delta_L$ and $\kappa_2\delta_L$ in red and blue respectively. Coinciding with the peak in S_d and the valley in the c profiles, we observe a sharp drop in average κ and κ_1 profiles just preceding $\xi/\delta_L = 0$ with $\kappa_2 \approx 0$ at minimum κ_1 - the quintessential signature of cylindrical flame-flame interaction shown in Fig. 2. This implies that due to their ubiquity at large Ka, localized, cylindrical flame-flame interaction precedes the nearly flat locations of the flame surface in the direction of reactants, on average. Since the cylindrical flame-flame interaction enhances S_d, the interacting iso-scalar surfaces approach each other faster, in turn separating the trailing surfaces leading to local broadening. The local flame thickening of these turbulent flame segments is found to be mainly due to the upstream flame-flame interaction. The results presented in Fig. 12a and c for Le08Ka1000 and Fig. 13a and c Le1Ka100 show qualitatively similar mean structures along the positive normal direction at $\xi/\delta_L = 0$.

Fig. 11b shows that just downstream, for $\xi/\delta_L > 0$, the maximum heat release rate of the averaged flame structure is enhanced to around 3.5 times the maximum standard laminar value. This results in an increased temperature gradient at $\kappa = 0$ ($\xi/\delta_L = 0$), causing the $\widetilde{S}_d$ to increase. The lean hydrogen-air turbulent flames at $\kappa = 0$ thus exhibit an enhancement in $\widetilde{S}_d$ at sub-unity Le. This will be discussed in detail later in the subsection 3.3.2. However, the normalized heat release rate profiles for Le08Ka1000 (Fig. 12b) and Le1Ka100 (Fig. 13b) are different from Le05Ka100 given their Le are close to unity and are also discussed in the subsection 3.3.2.

We visualize the non-local flame-flame interaction upstream of $\kappa = 0$ in Fig. 14 presenting segments of the iso-scalar surfaces at an instant of time for Le05Ka100 using both isotherms and iso-Y_{H_2} surfaces in (a) and (b), respectively. The iso-scalar surfaces are colored with S_d/S_L as shown by the colorscale at the bottom. The black markers denote the $\kappa = 0$ points on

$c_0 = 0.4$ and $c_Y = 0.7$ iso-surfaces. From the viewpoint of an observer in these nearly flat yet strained locations (black markers), the flame-flame interaction at the neighboring, highly curved, near cylindrical surfaces increases S_d at those corresponding neighboring surfaces. This causes those neighboring surfaces to separate faster from the reference resulting in flame thickening characterized by diminished scalar gradients.

3.3.2. Non-local effect of positive curvatures on $\widetilde{S}_d$ at $\kappa\delta_L = 0$

The previous section discussed how the cylindrical flame-flame interactions upstream (i.e. towards the reactant side) of the zero-curvature regions lead to departure from the local laminar flame structure. Shifting our focus to the region downstream (i.e. towards the product side) of the zero-curvature in the direction along the local normal estimated at $\xi/\delta_L = 0$, we observe that overall temperature (or c) is enhanced for Le05Ka100 (Fig. 11a) resulting in enhanced temperature gradient at $\xi/\delta_L = 0$ at all c_0. As mentioned before, the peak heat release rate is around 3.5 times the maximum laminar value for Le05Ka100 for all c_0 as shown in Fig. 11b. However, for L08Ka1000 with $Le = 0.76$, $\widehat{HRR} < 1$ for $c_0 = 0.05$ and 0.2 (Fig. 12b) given that the preheat zone is highly disrupted by the intense turbulence. For $c_0 = 0.4$ and $c_0 = 0.6$ the $\widehat{HRR} \approx 1.5$. In the preheat zone ($c_0 = 0.05$ and 0.2), the diffusion term contributes majorly to S_d while for $c_0 = 0.4$ and $c_0 = 0.6$ close to or beyond peak heat release rate the reaction term dominates (see Eq. (4)). In either case, with increasing c_0, the difference between the S_d/S_L and $S_d|_L/S_L$ decreases on the downstream of $\xi/\delta_L = 0$. The mean local flame structures for Le1Ka100 show similar behavior downstream of $\xi/\delta_L = 0$ (Fig. 13a and b). For all the cases, the non-dimensionalized tangential strain rate, $a_T\delta_L S_L$ is positive for $\xi/\delta_L \geq 0$. Interestingly, just downstream of $\xi/\delta_L = 0$, the flame surfaces are also near cylindrical with maximum principal curvature contributing majorly to the local curvature ($\kappa\delta_L = \kappa_1\delta_L + \kappa_2\delta_L \approx \kappa_1\delta_L, \kappa_2\delta_L \approx 0$) for all the cases. It seems that this large curvature and/or the existing tangential strain rate downstream contribute significantly to a large positive stretch. The positive stretching and preferential diffusion downstream leads to an enhanced heat release rate, eventually increasing temperature gradient and S_d. This effect is in addition to the existing tangential strain rate at $\kappa = 0$.

To isolate the effect of strain rate on increased heat release rate downstream of $\xi/\delta_L = 0$ we investigate conditionally averaged local flame structures along the local normal directions from the flame surface $c = c_0$ where

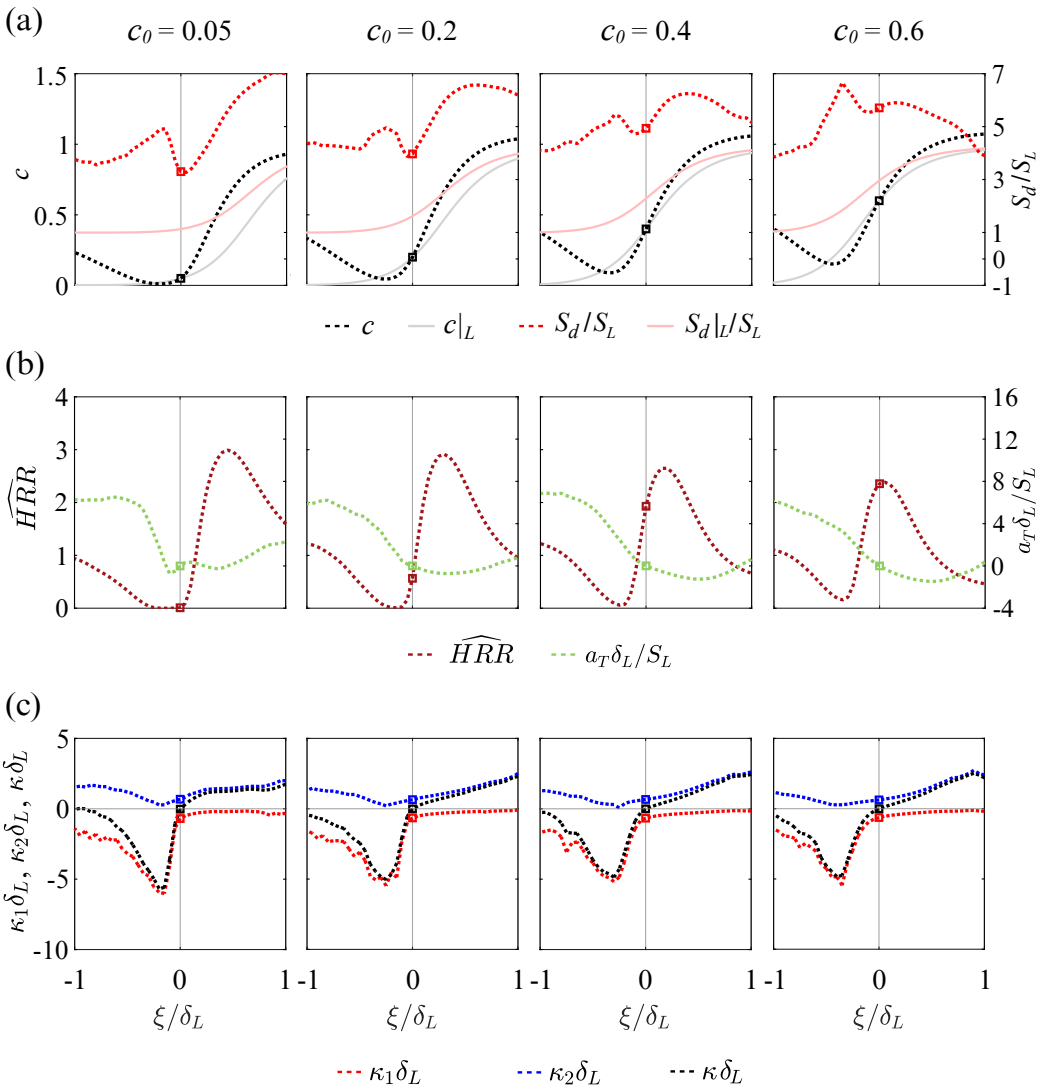

Figure 15: Mean local flame structures of (a) c and S_d/S_L (b) normalized heat release rate, $\widehat{HRR}$ and non-dimensional tangential strain rate, $a_T\delta_L/S_L$ (c) non-dimensional curvature $\kappa\delta_L$, non-dimensional minimum and maximum principal curvatures, $\kappa_1\delta_L$ and $\kappa_2\delta_L$ conditioned on κ = 0 and a_T = 0 at $c = c_0$ for Le05Ka100. The faint red and gray curves in the background in (a) represent the corresponding standard laminar flame structures.

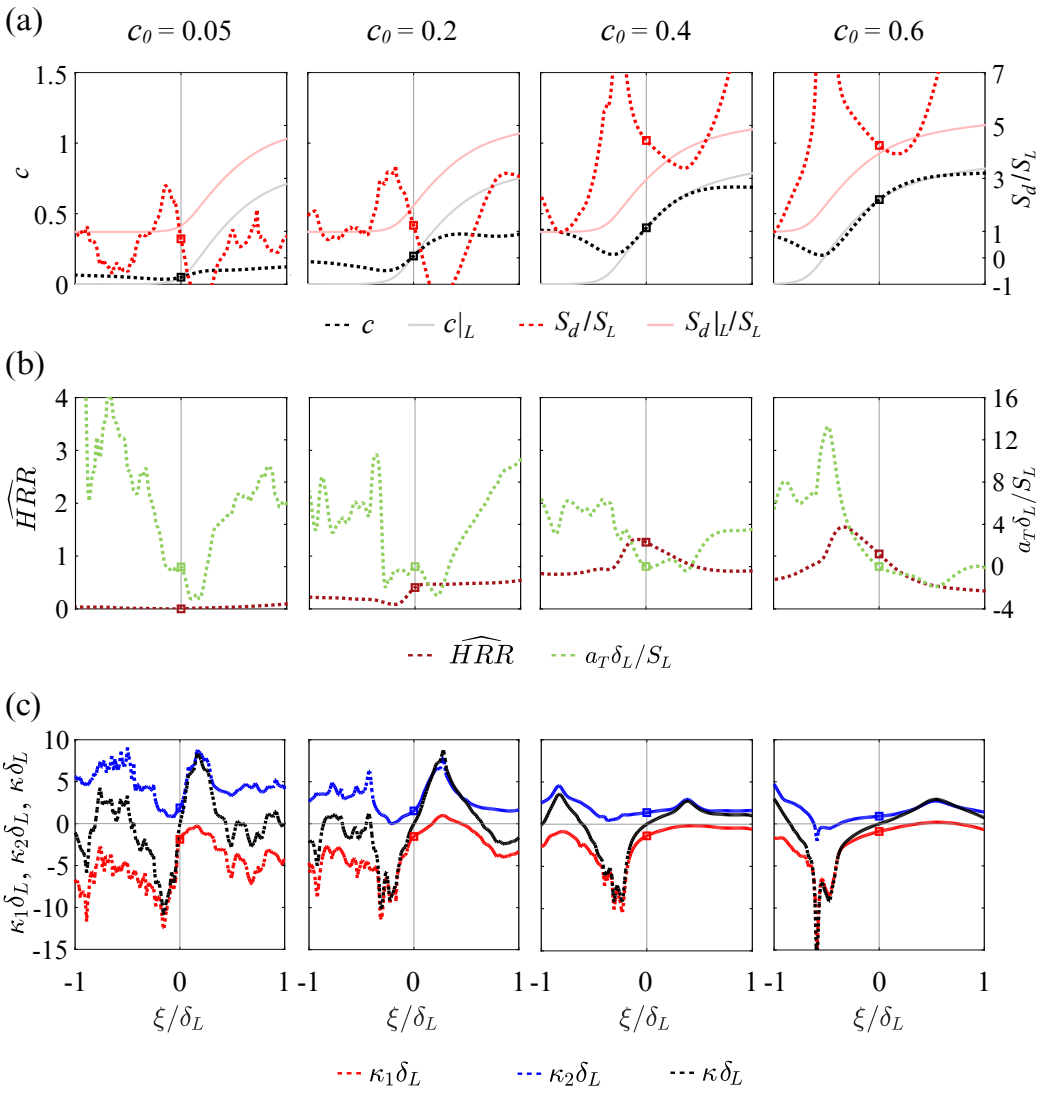

Figure 16: Mean local flame structures of (a) c and S_d/S_L (b) normalized heat release rate, $\widehat{HRR}$ and normalized tangential strain rate, $a_T\delta_L/S_L$ (c) non-dimensional curvature $\kappa\delta_L$, non-dimensional minimum and maximum principal curvatures, $\kappa_1\delta_L$ and $\kappa_2\delta_L$ conditioned on κ = 0 and a_T = 0 at $c = c_0$ for Le08Ka1000. The faint red and gray curves in the background in (a) represent the corresponding standard laminar flame structures.

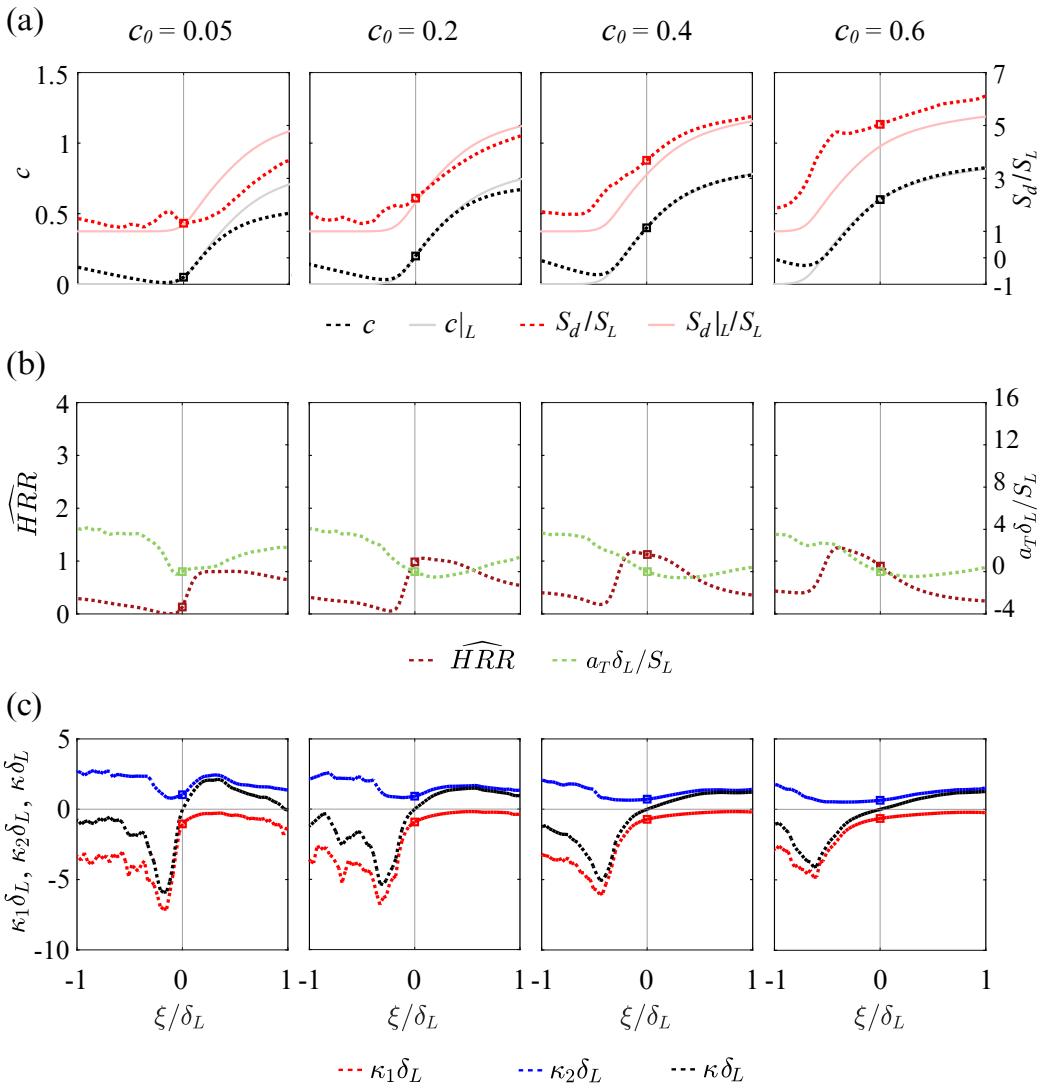

Figure 17: Mean local flame structures of (a) c and S_d/S_L (b) normalized heat release rate, $\widehat{HRR}$ and normalized tangential strain rate, $a_T\delta_L/S_L$ (c) non-dimensional curvature $\kappa\delta_L$, non-dimensional minimum and maximum principal curvatures, $\kappa_1\delta_L$ and $\kappa_2\delta_L$ in conditioned on $\kappa = 0$ and $a_T = 0$ at $c = c_0$ for Le1Ka100. The faint red and gray curves in the background in (a) represent the corresponding standard laminar flame structures.

$\kappa = a_T = 0$. The points on the flame surface conditioned on $a_T = 0$ are filtered over the range $-0.1 < a_T\delta_L/S_L < 0.1$ for Le05Ka100 and Le1Ka100 whereas given the intense tangential straining at $Ka \sim \mathcal{O}(1000)$ fewer points are obtained on the flame surface for the given range of $a_T\delta_L/S_L$, hence to achieve statistical convergence of the structures we increase the range to $-0.5 < a_T\delta_L/S_L < 0.5$ for Le08Ka1000.

Figures 15, 16 and 17 present the mean local flame structures based on (a) S_d/S_L (red), c (black) (b) $\widehat{HRR}$ (dark red), $a_T\delta_L/S_L$ (green) (c) $\kappa_1\delta_L$ (red), $\kappa_2\delta_L$ (blue), $\kappa_2\delta_L$ (black) conditioned on $\kappa = a_T = 0$ for $c_0 = 0.05, 0.2, 0.4$ and 0.6 in dotted curves for Le05Ka100, Le08Ka1000 and Le1Ka100 respectively. For Le05Ka100 the nature of structures based on S_d/S_L, c, $\widehat{HRR}$, $\kappa\delta_L$, $\kappa_1\delta_L$ and $\kappa_2\delta_L$ qualitatively resemble those presented in Fig. 11. The $S_d > S_d|_L$ at $\xi/\delta_L = 0$ for all c_0. The temperature gradient is also higher than the laminar counterpart at $\xi/\delta_L = 0$. On the other hand, for $0 < \xi/\delta_L \leq 1$, $a_T\delta_L/S_L$ attains very small values, close to zero. In addition, $\kappa\delta_L \approx \kappa_2\delta_L$, i.e., the cylindrical shape of the flame surface with positive curvature, is retained just downstream of $\xi/\delta_L = 0$. This shows that the enhanced heat release rate caused by preferential diffusion at the positive stretch rate is contributed majorly by positive curvature rather than the tangential strain rate a_T. Since the $Le \approx 0.5$, the molecular diffusivity of hydrogen exceeds that of the thermal diffusivity of the ultra-lean mixture. Thus, such near cylindrical regions with positive curvature ($\kappa\delta_L > 1$) allow the focusing of species diffusion from low-temperature regions into the higher ones. This results in enhanced heat released rate and consequently increased temperature and the resulting gradient leading to enhanced $\widetilde{S}_d$ at $\xi/\delta_L = 0$. Thus the enhancement of $\widetilde{S_{d,0}}$ conditioned on zero tangential strain rate over S_L (black hollow square in Fig. 2) is attributed majorly to preferential diffusion at positively curved regions. It should be noted that though the preexisting history effects are not the focus of the present study, we acknowledge their possible contribution to enhancement in S_d as well [74].

Based on the investigation of the mean local flame structures at zero-curvature points Howarth et al. [18] reported enhanced temperature and heat release rate at zero-curvature regions lying on the mass fraction based iso-scalar surface with $c_0 = 0.9$. The local flame structures were obtained along the paths normal to the flame surface following the gradients of the mass fraction and then averaged to obtain the corresponding mean local flame structure [53]. Given the definition of the constructed path on which the structures were obtained, non-local flame-flame interaction upstream of

$\xi/\delta_L = 0$ was not captured in their analysis. The present finding that enhanced heat release rate due to preferential diffusion at large positively curved regions leads to faster propagation of the flame locally ($\xi/\delta_L = 0$) is in agreement with Howarth et al. [18]. However, it was argued by Howarth et al. [18] that after the passage of these positively curved leading points, a wake region with low curvature remains, which is still at superadiabatic temperatures sustaining higher reaction rates than the corresponding laminar case. This results in propagation speeds exceeding S_L. Here, we find that in the conditionally averaged structure we obtained, it is the positively curved near cylindrical regions and not leading points that are spherical that experience enhanced burning. Moreover, such regions are present downstream of the zero-curvature regions in the conditionally averaged flame structure. The triple conditioned mean local flame structure based on S_d/S_L, c, $\widetilde{HRR}$, $\kappa\delta_L$, $\kappa_1\delta_L$, $\kappa_2\delta_L$ for Le08Ka1000 and Le1Ka100 in Fig. 16 and Fig. 17 also resemble their double conditioned counterparts in presented in Fig. 12 and Fig. 13 respectively. Near cylindrical positively curved regions are also present with $a_T\delta_L/S_L \approx 0$ in the near vicinity of $\xi/\delta_L = 0$ in the downstream of it for both cases at all c_0. Since the Le is close to unity, a temperature gradient less than ($c_0 = 0.05$ and 0.2) or equal ($c_0 = 0.4$ and 0.6) to the laminar case at $\xi/\delta_L = 0$ is observed for Le08Ka100. For Le1Ka100 at $c_0 = 0.4$ and 0.6 lying beyond c_0 for maximum heat release rate, we observe $S_d > S_d|_L$ at $\xi/\delta_L = 0$ this is due to the increased contribution from the heat release term to S_d compared to the diffusion term (see Eq. (4)).

Finally, it is noteworthy to mention that although planar laminar flames under tangential straining with increased gradients are faster than the standard laminar flame, they do not experience the effect of preferential diffusion at positive curvatures. On the other hand, turbulent flame surfaces with zero-curvatures experience enhanced $\widetilde{S}_d$ majorly due to the non-local Le effect rather than the local tangential strain rate. Therefore, the regions with $\kappa = 0$ on a turbulent flame surface, on average, can propagate faster than the canonical form under the same tangential strain rates. We observe this for the c_0 lying beyond the peak heat release rate, i.e., $c_0 = 0.6$ for Le08Ka1000 and $c_0 = 0.4, 0.6$ for Le1Ka100 (see Fig. 5b and c). Thus, due to the distinct nature of the mean local flame structure, including the underlying mechanism for $\widetilde{S}_d$ enhancement at zero-curvature regions in turbulent flames, the standalone CFF may not be the best model for predicting $\widetilde{S_{d,0}}$ under the same tangential strain rate condition.

4. Conclusions

Localized cylindrical flame-flame interaction at large negative curvatures leads to enhanced flame displacement speeds in near unity Lewis number lean hydrogen-air turbulent flames. Analytical or numerical interaction models can explain such large excursions of S_d. The present study investigates the behavior of $\widetilde{S}_d$ at large negative curvatures in preferentially diffusive ultra-lean H_2-air turbulent flames and further explores its implications paired with the Lewis number effect on the mean local flame structure and consequently the mean local flame displacement speed at zero-curvature.

To that end, three 3D DNS datasets at varying Le and Ka are investigated to understand the $\widetilde{S}_d$ at large negative curvatures as well as at zero-curvatures. Detailed reaction mechanisms [57, 80] are used to model the chemistry for all the datasets. Strong negative flame stretch led to an extremely low heat release rate during flame-flame interaction at large negative curvature. This resulted in a near-perfect agreement of mean $\widetilde{S}_d$ conditioned on curvature with the interaction model in the asymptotic limit of large negative curvature.

In addition, it is found that most parts of ultra-lean, large Ka hydrogen flames, characterized by $\kappa \approx 0$, propagate faster in turbulence when compared to their standard laminar counterpart due to preferential diffusion effects. However, the canonical configuration of a steady laminar strained flame was insufficient in quantifying and explaining such enhancement. Mapping flame displacement speed (ratios) with the local structure represented by the thermal gradient (ratios), the reason for this difference systematically emerges. All the investigated turbulent flames, irrespective of Le and Ka, possess unique mean local flame structures in the zero-curvature regions. At zero-curvatures, local broadening persists due to a reversed flame speed gradient resulting from the non-local cylindrical flame-flame interaction with negative curvature upstream in the positive normal direction. The severity of this effect however depends on the Ka. This effect is paired with an increased local temperature gradient resulting from preferential diffusion at the positively curved near cylindrical regions downstream of zero-curvature regions, imparting the turbulent premixed flame its distinct mean local structure and the local flame speed at these points. This work thus highlights for the first time that mean local flame structure in turbulence results from the aforementioned non-local effects rather than just local tangential straining present in the canonical configurations.

5. Acknowledgement

This research was supported in part by the Natural Sciences and Engineering Research Council of Canada through a Discovery Grant and by King Abdullah University of Science and Technology (KAUST). Computational resources were provided by the SciNet High-Performance Computing Consortium at the University of Toronto and the Digital Research Alliance of Canada (the Alliance).

Appendix A. Scaling analysis

$$S_d = \frac{1}{\rho C_p}\left[\underbrace{\frac{\nabla\cdot(\lambda'\nabla T)}{|\nabla T|}}_{T_1} \quad \underbrace{-\frac{\rho\nabla T\cdot\sum_k(C_{p,k}V_kY_k)}{|\nabla T|}}_{T_2} \underbrace{-\frac{\sum_k h_k\dot{\omega}_k}{|\nabla T|}}_{T_3}\right] \tag{A.1}$$

A term-by-term analysis is performed for Eq. (A.1), where λ', V_k, h_k and $\dot{\omega}_k$ are the thermal conductivity of the mixture, the molecular diffusion velocity, enthalpy, and net production rate of the kth species at a given isotherm, respectively. $C_{p,k}$ and C_p are the constant-pressure specific heat for the kth species and the bulk mixture using the mixture-averaged formula. The terms T_1, T_2 and T_3 represent the contributions from heat conduction, heat transfer by mass diffusion and reaction, respectively. For an isotherm lying in the preheat zone far from the heat release layers, we can assume $\sum_k h_k\dot{\omega}_k = 0$. Existing literature found [8, 35] T_2 to be an order of magnitude smaller than T_1 and T_3 and can be assumed negligible. Thus decomposing T_1 [22] we get,

$$S_d \approx \frac{1}{\rho C_p}\left[-\lambda'\kappa - \frac{\lambda'}{|\nabla T|}\boldsymbol{n}\cdot\nabla(|\nabla T|)\right] \tag{A.2}$$

Using $\boldsymbol{n}$ as the local unit normal vector, we substitute $|\nabla T| = -\partial T/\partial n$ and $\boldsymbol{n}\cdot\nabla = \partial/\partial n$. Now, S_d for an isotherm surface, c_0 at $\kappa = 0$ can be written as,

$$S_d|_{\kappa=0} \approx -\alpha\frac{\partial^2 T/\partial n^2|_{\kappa=0}}{\partial T/\partial n|_{\kappa=0}} \tag{A.3}$$

Using scaling relationship as $\partial^2 T/\partial n^2 \sim \Delta T/\delta_p^2$ and $\partial T/\partial n \sim \Delta T/\delta_p$. ΔT and δ_p are the characteristic temperature rise and local flame thickness in the preheat zone at $\kappa = 0$. Since $S_{d,0} = \langle S_d|_{\kappa=0} \rangle$, we get $S_{d,0} \sim \alpha/\delta_p$.

Applying density-weighing and normalizing by the corresponding laminar counterpart, we get Eq. (A.4)

$$\frac{S_{d,0}}{S_{L,c_0}} = \frac{\widetilde{S_{d,0}}}{S_L} \approx \frac{\delta_p}{\delta_{p,0}} \approx \frac{|\nabla c|_{c_0}|_{\kappa=0}}{|\nabla c|_{c_0,L}} \approx |\widehat{\nabla c}|_{c_0}|_{\kappa=0} \tag{A.4}$$

Here the characteristic thickness is assumed to be inversely proportional to the local gradient i.e. $\delta_p = (c_0 - c_{min})/|\nabla c|_{c_0} = c_0/|\nabla c|_{c_0}$ [38, 47] similar to $\delta_L = (c_{max} - c_{min})/|\nabla c|_{max} = 1/|\nabla c|_{max}$.

References

[1] S. Gkantonas, M. Talibi, R. Balachandran, E. Mastorakos, Hydrogen combustion in gas turbines, Hydrogen for Future Thermal Engines (2023) 407–428.

[2] T. Echekki, J. H. Chen, Unsteady strain rate and curvature effects in turbulent premixed methane-air flames, Combust. Flame 106 (1996) 184–190.

[3] T. Echekki, J. H. Chen, Analysis of the contribution of curvature to premixed flame propagation, Combust. Flame 118 (1999) 308–311.

[4] H. G. Im, J. H. Chen, Effects of flow transients on the burning velocity of laminar hydrogen/air premixed flames, Proc. Combust. Inst. 28 (2000) 1833–1840.

[5] J. H. Chen, H. G. Im, Correlation of flame speed with stretch in turbulent premixed methane/air flames, Symp. (Int.) Combust. 27 (1998) 819–826.

[6] L. Cifuentes, C. Dopazo, A. Sandeep, N. Chakraborty, A. Kempf, Analysis of flame curvature evolution in a turbulent premixed bluff body burner, Phys. Fluids 30 (2018) 095101.

[7] N. Chakraborty, R. S. Cant, Effects of strain rate and curvature on surface density function transport in turbulent premixed flames in the thin reaction zones regime, Phys. Fluids 17 (2005) 065108.

[8] H. A. Uranakara, S. Chaudhuri, H. L. Dave, P. G. Arias, H. G. Im, A flame particle tracking analysis of turbulence–chemistry interaction in hydrogen–air premixed flames, Combust. Flame 163 (2016) 220–240.

[9] H. A. Uranakara, S. Chaudhuri, K. N. Lakshmisha, On the extinction of igniting kernels in near-isotropic turbulence, Proc. Combust. Inst. 36 (2017) 1793–1800.

[10] N. Peters, P. Terhoeven, J. H. Chen, T. Echekki, Statistics of flame displacement speeds from computations of 2-d unsteady methane-air flames, Symp. (Int.) Combust. 27 (1998) 833–839.

[11] N. Chakraborty, R. Cant, Influence of lewis number on curvature effects in turbulent premixed flame propagation in the thin reaction zones regime, Phys. Fluids 17 (2005).

[12] D. C. Haworth, T. J. Poinsot, Numerical simulations of lewis number effects in turbulent premixed flames, J. Fluid Mech. 244 (1992) 405–436.

[13] C. Rutland, A. Trouvé, Direct simulations of premixed turbulent flames with nonunity lewis numbers, Combust. Flame 94 (1993) 41–57.

[14] A. Alqallaf, M. Klein, N. Chakraborty, Effects of lewis number on the evolution of curvature in spherically expanding turbulent premixed flames, Fluids 4 (2019) 12.

[15] R. Sankaran, E. R. Hawkes, C. S. Yoo, J. H. Chen, Response of flame thickness and propagation speed under intense turbulence in spatially developing lean premixed methane–air jet flames, Combust. Flame 162 (2015) 3294–3306.

[16] A. Amato, M. Day, R. K. Cheng, J. Bell, D. Dasgupta, T. Lieuwen, Topology and burning rates of turbulent, lean, h2/air flames, Combust. Flame 162 (2015) 4553–4565.

[17] A. Amato, Leading points concepts in turbulent premixed combustion modeling, Ph.D. thesis, Georgia Institute of Technology, 2014.

[18] T. Howarth, E. Hunt, A. Aspden, Thermodiffusively-unstable lean premixed hydrogen flames: Phenomenology, empirical modelling, and thermal leading points, Combust. Flame 253 (2023) 112811.

[19] S. Chaudhuri, Life of flame particles embedded in premixed flames interacting with near isotropic turbulence, Proc. Combust. Inst. 35 (2015) 1305–1312.

[20] H. L. Dave, A. Mohan, S. Chaudhuri, Genesis and evolution of premixed flames in turbulence, Combust. Flame 196 (2018) 386–399.

[21] Ya. B. Zeldovich, G. I. Barenblatt, V. B. Librovich, G. M. Makhviladze, Mathematical theory of combustion and explosions, Consultants Bureau, New York, NY, 1985.

[22] H. L. Dave, S. Chaudhuri, Evolution of local flame displacement speeds in turbulence, J. Fluid Mech. 884 (2020) A46.

[23] J. Bechtold, M. Matalon, The dependence of the markstein length on stoichiometry, Combust. Flame 127 (2001) 1906–1913.

[24] G. K. Giannakopoulos, M. Matalon, C. E. Frouzakis, A. G. Tomboulides, The curvature markstein length and the definition of flame displacement speed for stationary spherical flames, Proc. Combust. Inst. 35 (2015) 737–743.

[25] G. K. Giannakopoulos, A. Gatzoulis, C. E. Frouzakis, M. Matalon, A. G. Tomboulides, Consistent definitions of "flame displacement speed" and "markstein length" for premixed flame propagation, Combust. Flame 162 (2015) 1249–1264.

[26] N. Peters, Turbulent Combustion, Cambridge University Press, 2000.

[27] N. Chakraborty, R. S. Cant, Direct numerical simulation analysis of the flame surface density transport equation in the context of large eddy simulation, Proc. Combust. Inst. 32 (2009) 1445–1453.

[28] A. Haghiri, M. Talei, M. J. Brear, E. R. Hawkes, Sound generation by turbulent premixed flames, J. Fluid Mech. 843 (2018) 29–52.

[29] D. Brouzet, A. Haghiri, M. Talei, M. J. Brear, Annihilation events topology and their generated sound in turbulent premixed flames, Combust. Flame 204 (2019) 268–277.

[30] T. D. Dunstan, N. Swaminathan, K. N. C. Bray, N. G. Kingsbury, Flame interactions in turbulent premixed twin v-flames, Combust. Sci. Technol. 185 (2013) 134–159.

[31] R. Griffiths, J. Chen, H. Kolla, R. Cant, W. Kollmann, Three-dimensional topology of turbulent premixed flame interaction, Proc. Combust. Inst. 35 (2015) 1341–1348.

[32] S. Trivedi, R. Griffiths, H. Kolla, J. H. Chen, R. S. Cant, Topology of pocket formation in turbulent premixed flames, Proc. Combust. Inst. 37 (2019) 2619–2626.

[33] A. Haghiri, M. Talei, M. Brear, E. Hawkes, Flame annihilation displacement speed and stretch rate in turbulent premixed flames, Flow Turbul. Combust. 104 (2020) 977–996.

[34] Yuvraj, Y. N. Ardebili, W. Song, H. G. Im, C. K. Law, S. Chaudhuri, et al., On flame speed enhancement in turbulent premixed hydrogen-air flames during local flame-flame interaction, Combust. Flame 257 (2023) 113017.

[35] Yuvraj, W. Song, H. Dave, H. G. Im, S. Chaudhuri, et al., Local flame displacement speeds of hydrogen-air premixed flames in moderate to intense turbulence, Combust. Flame 236 (2022) 111812.

[36] S. Pope, P. Yeung, S. Girimaji, The curvature of material surfaces in isotropic turbulence, Phys. Fluids A: Fluid Dynamics 1 (1989) 2010–2018.

[37] T. Zheng, J. You, Y. Yang, Principal curvatures and area ratio of propagating surfaces in isotropic turbulence, Phys. Rev. Fluids 2 (2017) 103201.

[38] P. E. Hamlington, A. Y. Poludnenko, E. S. Oran, Intermittency in premixed turbulent reacting flows, Phys. Fluids 24 (2012) 075111.

[39] P. E. Hamlington, A. Y. Poludnenko, E. S. Oran, Interactions between turbulence and flames in premixed reacting flows, Phys. Fluids 23 (2011) 125111.

[40] P. E. Hamlington, A. Y. Poludnenko, E. S. Oran, Turbulence and scalar gradient dynamics in premixed reacting flows, in: 40th Fluid Dynamics Conference and Exhibit, 2010, p. 5027.

[41] A. Y. Poludnenko, E. Oran, The interaction of high-speed turbulence with flames: Global properties and internal flame structure, Combust. Flame 157 (2010) 995–1011.

[42] A. Poludnenko, E. Oran, The interaction of high-speed turbulence with flames: Turbulent flame speed, Combust. Flame 158 (2011) 301–326.

[43] W. Song, F. E. Hernandez-Perez, E. A. Tingas, H. G. Im, Statistics of local and global flame speeds for turbulent H2/air premixed flames at high Karlovitz numbers, Combust. Flame 232 (2021) 111523.

[44] A. Lipatnikov, V. Sabelnikov, F. Hernández-Pérez, W. Song, H. G. Im, Prediction of mean radical concentrations in lean hydrogen-air turbulent flames at different karlovitz numbers adopting a newly extended flamelet-based presumed pdf, Combust. Flame 226 (2021) 248–259.

[45] A. M. Steinberg, P. E. Hamlington, X. Zhao, Structure and dynamics of highly turbulent premixed combustion, Prog. Energy Combust. Sci. 85 (2021) 100900.

[46] L. K. Su, N. T. Clemens, The structure of fine-scale scalar mixing in gas-phase planar turbulent jets, J. Fluid Mech. 488 (2003) 1–29.

[47] S. Chaudhuri, H. Kolla, H. L. Dave, E. R. Hawkes, J. H. Chen, C. K. Law, Flame thickness and conditional scalar dissipation rate in a premixed temporal turbulent reacting jet, Combust. Flame 184 (2017) 273–285.

[48] A. Lipatnikov, J. Chomiak, Molecular transport effects on turbulent flame propagation and structure, Prog. Energy Combust. Sci. 31 (2005) 1–73.

[49] S. Chaudhuri, V. Akkerman, C. K. Law, Spectral formulation of turbulent flame speed with consideration of hydrodynamic instability, Phys. Rev. E 84 (2011) 026322.

[50] J. Chomiak, A. N. Lipatnikov, Simple criterion of importance of laminar flame instabilities in premixed turbulent combustion of mixtures characterized by low lewis numbers, Phys. Rev. E 107 (2023) 015102.

[51] L. Berger, A. Attili, H. Pitsch, Synergistic interactions of thermodiffusive instabilities and turbulence in lean hydrogen flames, Combust. Flame 244 (2022) 112254.

[52] M. Rieth, A. Gruber, J. H. Chen, The effect of pressure on lean premixed hydrogen-air flames, Combust. Flame 250 (2023) 112514.

[53] T. Howarth, A. Aspden, An empirical characteristic scaling model for freely-propagating lean premixed hydrogen flames, Combust. Flame 237 (2022) 111805.

[54] M. Matalon, C. Cui, J. K. Bechtold, Hydrodynamic theory of premixed flames: effects of stoichiometry, variable transport coefficients and arbitrary reaction orders, J. Fluid Mech. 487 (2003) 179–210.

[55] S. B. Pope, Turbulent Flows, Cambridge University Press, 2000.

[56] The Collaboration, A. Brandenburg, A. Johansen, P. Bourdin, W. Dobler, W. Lyra, M. Rheinhardt, S. Bingert, N. Haugen, A. Mee, F. Gent, N. Babkovskaia, C.-C. Yang, T. Heinemann, B. Dintrans, D. Mitra, S. Candelaresi, J. Warnecke, P. Käpylä, A. Schreiber, P. Chatterjee, M. Käpylä, X.-Y. Li, J. Krüger, J. Aarnes, G. Sarson, J. Oishi, J. Schober, R. Plasson, C. Sandin, E. Karchniwy, L. Rodrigues, A. Hubbard, G. Guerrero, A. Snodin, I. Losada, J. Pekkilä, C. Qian, The pencil code, a modular mpi code for partial differential equations and particles: multipurpose and multiuser-maintained, J. Open Source Softw. 6 (2021) 2807.

[57] J. Li, Z. Zhao, A. Kazakov, F. Dryer, An updated comprehensive kinetic model of hydrogen combustion, Int. J. Chem. Kinet. 36 (2004) 566 – 575.

[58] C. K. Law, Combustion Physics, Cambridge University Press, 2006.

[59] J. Schlup, G. Blanquart, Validation of a mixture-averaged thermal diffusion model for premixed lean hydrogen flames, Combust. Theory Model. 22 (2018) 264–290.

[60] W. Song, F. E. Hernández-Pérez, H. G. Im, Diffusive effects of hydrogen on pressurized lean turbulent hydrogen-air premixed flames, Combust. Flame 246 (2022) 112423.

[61] A. Aspden, M. Day, J. Bell, Lewis number effects in distributed flames, Proc. Combust. Inst. 33 (2011) 1473–1480.

[62] J. F. Grcar, J. B. Bell, M. S. Day, The soret effect in naturally propagating, premixed, lean, hydrogen–air flames, Proc. Combust. Inst. 32 (2009) 1173–1180.

[63] R. J. Kee, J. F. Grcar, M. D. Smooke, J. A. Miller, E. Meeks, PREMIX: A fortran program for modeling steady laminar one-dimensional premixed flames, Sandia National Labs., Livermore, CA, USA (1985).

[64] S. Chaudhuri, B. Savard, Turbulent flame speed based on the mass flow rate: Theory and dns, Combust. Flame 252 (2023) 112735.

[65] H. Chu, L. Berger, T. Grenga, Z. Wu, H. Pitsch, Effects of differential diffusion on hydrogen flame kernel development under engine conditions, Proc. Combust. Inst. (2022).

[66] P. Yeung, S. Girimaji, S. Pope, Straining and scalar dissipation on material surfaces in turbulence: Implications for flamelets, Combust. Flame 79 (1990) 340–365.

[67] S. Pope, The evolution of surfaces in turbulence, Int. J. Eng. Sci. 26 (1988) 445–469.

[68] S. S. Girimaji, S. B. Pope, Propagating surfaces in isotropic turbulence, J.Fluid Mech. 234 (1992) 247–277.

[69] V. Coulon, J. Gaucherand, V. Xing, D. Laera, C. Lapeyre, T. Poinsot, Direct numerical simulations of methane, ammonia-hydrogen and hydrogen turbulent premixed flames, Combust. Flame 256 (2023) 112933.

[70] N. Detomaso, J.-J. Hok, O. Dounia, D. Laera, T. Poinsot, A generalization of the thickened flame model for stretched flames, Combust. Flame 258 (2023) 113080.

[71] E. R. Hawkes, J. H. Chen, Comparison of direct numerical simulation of lean premixed methane–air flames with strained laminar flame calculations, Combust. Flame 144 (2006) 112–125.

[72] H. Lee, P. Dai, M. Wan, A. N. Lipatnikov, A dns study of extreme and leading points in lean hydrogen-air turbulent flames - part ii: Local velocity field and flame topology, Combust. Flame 235 (2022) 111712.

[73] F. H. Vance, Y. Shoshin, L. De Goey, J. A. van Oijen, A physical relationship between consumption and displacement speed for premixed flames with finite thickness, Proc. Combust. Inst. 38 (2021) 2215–2223.

[74] H. Im, J. Bechtold, C. Law, Response of counterflow premixed flames to oscillating strain rates, Combust. Flame 105 (1996) 358–372.

[75] S. H. Kim, H. Pitsch, Scalar gradient and small-scale structure in turbulent premixed combustion, Phys. Fluids 19 (2007) 115104.

[76] R. Sankaran, E. R. Hawkes, J. H. Chen, T. Lu, C. K. Law, Structure of a spatially developing turbulent lean methane–air bunsen flame, Proc. Combust. Inst. 31 (2007) 1291–1298.

[77] C. Dopazo, L. Cifuentes, J. Martin, C. Jimenez, Strain rates normal to approaching iso-scalar surfaces in a turbulent premixed flame, Combust. Flame 162 (2015) 1729–1736.

[78] H. Wang, E. R. Hawkes, J. H. Chen, B. Zhou, Z. Li, M. Aldén, Direct numerical simulations of a high karlovitz number laboratory premixed jet flame – an analysis of flame stretch and flame thickening, J. Fluid Mech. 815 (2017) 511–536.

[79] N. Chakraborty, N. Swaminathan, Influence of the damköhler number on turbulence-scalar interaction in premixed flames. i. physical insight, Phys. Fluids 19 (2007).

[80] M. P. Burke, M. Chaos, Y. Ju, F. L. Dryer, S. J. Klippenstein, Comprehensive H2/O2 kinetic model for high-pressure combustion, Int. J. Chem. Kinet. 44 (2012) 444–474.